CHALMERS

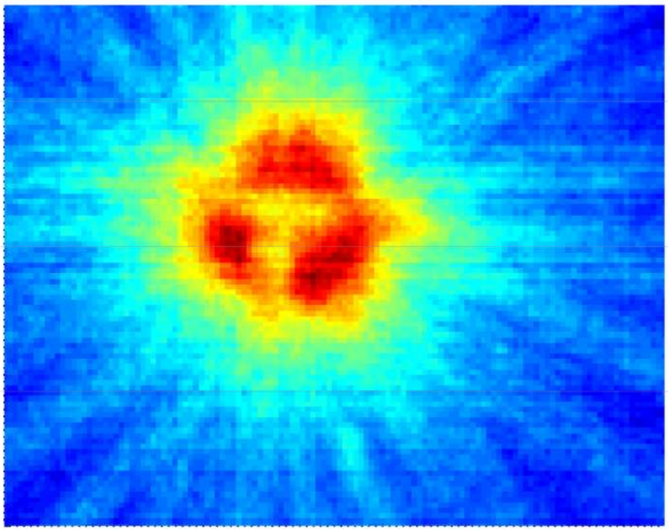

Ultra-low field Magnetic Resonance Imaging using high-T_c SQUIDs

Master of Science Thesis in Nanoscale Science and Technology

MAGNUS JÖNSSON

Department of Microtechnology and Nanoscience – MC2
CHALMERS UNIVERSITY OF TECHNOLOGY
Gothenburg, Sweden, 2011

Ultra-low field Magnetic Resonance Imaging using high-T_c SQUIDs

MAGNUS J. JÖNSSON

Department of Microtechnology and Nanoscience - MC2
CHALMERS UNIVERSITY OF TECHNOLOGY
Göteborg, Sweden 2012

Ultra-low field Magnetic Resonance Imaging using high-T_c SQUIDs
MAGNUS J. JÖNSSON

Quantum Device Physics Laboratory
Department of Microtechnology and Nanoscience - MC2
Chalmers University of Technology
SE-412 96 Göteborg
Sweden
Telephone: +46 (0)31-772 1000

Part of this work was made possible with the financial support from Kristina Stenborgs stiftelse and the European Commission Framework Program 7 (FP7/2007-2013) MEGMRI (grant agreement no 200859).

Cover Image: The acquired image of a T-shaped water phantom acquired at at 89.3 μT measurement field. The illustration on the right shows a cross-section of the phantom. For more information, see section 5.2.6.

Chalmers Reproservice
Göteborg, Sweden 2012

Ultra-low field Magnetic Resonance Imaging using high-T_c SQUIDs
MAGNUS JÖNSSON
Department of Microtechnology and Nanoscience - MC2
Chalmers University of Technology

Abstract A measurement system for ultra-low field Magnetic Resonance Imaging (ulf-MRI) has been built and programmed and a few proof-of-principle 2D images of water phantoms have been acquired at 89.3 μT measurement field. The smallest detectable volume of water has been determined to be 0.3 cm^3. A single-shot NMR spectrum of a water sample has been detected and the signal-to-noise ratio of the resonant peak has been determined to be 60 with a linewidth of 0.9 Hz at 3.8 kHz. A few different pulsing sequences have been tried and the most promising has been determined to be a prepolarization pulse that is turned off non-adiabatically.

Some obstacles towards building a full-fledged ulf-MRI measurement system have been identified and partially addressed, such as the external magnetic fluctuations of around 200 nT and that an unshielded SQUID detector has problems performing reliably after the prepolarization pulse.

Keywords: Magnetic Resonance Imaging, Nuclear Magnetic Resonance, Superconducting Quantum Interference Device, Ultra-low field NMR, Ultra-low field MRI, NMR, MRI, SQUID, ulf-NMR, ulf-MRI

Acknowledgements

This thesis would not have been possible without the support of more than a few people. First, I would like to thank Fredrik Öisjöen who has been a tremendous help during the whole project. His optimism and drive is unbeatable. I am also very grateful to Justin Schneiderman for his useful input and encouragement at times of despair.

Prof. Dag Winkler has also been been a great help, sometimes coming up with beautiful and complex solutions to problems, and his experience and input has been invaluable. I would also like to thank Alexei Kalaboukhov who has been a great resource when experiencing problems with anything SQUID-related.

Last but not least, I would like to thank my family who have always supported me during my years studying physics.

Magnus Jönsson

Contents

1 Introduction

The main goal for my thesis has been to detect an ultra-low field Nuclear Magnetic Resonance (ulf-NMR) signal from water and take the first steps towards achieving ultra-low field Magnetic Resonance Imaging (ulf-MRI).

1.1 MRI

Since its invention in the 1970s, MRI has proven to be a valuable tool for imaging the soft tissues inside the body. In conventional (high-field) MRI, the faraday detectors used are sensitive to the change in magnetic signal, $\frac{\partial B}{\partial t}$ [1]. If we combine this with the fact that the magnetization of the sample is linear compared to the applied magnetic field, we find that the signal scales as B^2. This means that manufacturers of MRI systems want as high a field as possible. But higher fields also set stricter requirements on the field homogeniety, and leads to higher cost of the entire system, so most manufacturers deliver systems at 1.5 or 3 T.

Already in the early 1990s Seton et al. [2] used a Superconducting Quantum Interference Device (SQUID) to perform NMR measurements on room-temperature water samples. They demonstrated that using a SQUID for detecting the magnetic signal at low frequencies may be beneficial, for example allowing use of certain radio frequency pulse sequences that cause tissue heating in high-field MRI. In 1997 they demonstrated the capabilities of a SQUID-based system by imaging a human arm [3].

McDermott et al. [4] have demonstrated that by first applying a high prepolarization field over the sample and then measuring at a lower field (in the order of μT), you can have an inhomogeniety in the field of 1% which simplifies the design of the coil drastically. They observed that a narrow linewidth means a high signal-to-noise ratio in the NMR spectrum and thus higher imaging resolution is possible, see figure 1. This means that in some cases ultra-low field MRI has a chance to compete with its high-field counterpart.

Clarke et al. [5] are currently conducting experiments where they use ulf-MRI to diagnose prostate cancer. They have received some promising *in vitro* results and are currently preparing for *in vivo* measurements.

In high-field MRI, the presence of metal can distort the image because of screening currents in said metal. Mößle et al. [6] have shown that this problem does not seem to exist in ulf-MRI, since the frequency is lower. Said research group also showed that ulf-MRI is able to image inside a metal can, which might indicate applications for quality control in the food industry.

Note that these discoveries have been made at the same research group at University of California, Berkeley. At the Los Alamos National Laboratory, Zotev et al. [17] have created a system of their own and even published the first ulf-MRI images of a human brain. An ongoing research project also

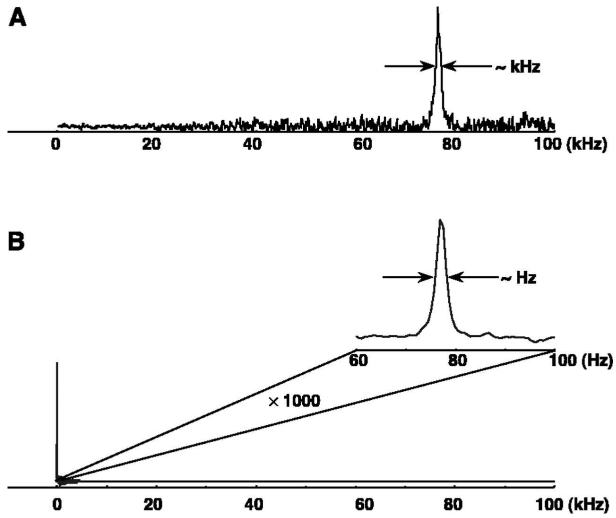

Figure 1: a) NMR spectrum of 5 ml mineral oil acquired in a measurement field of 1.8 mT. Average of 10 000 measurements. b) NMR spectrum of 5 ml mineral oil acquired in a measurement field of 1.8 μT, with a prepolarization pulse of 2 mT. Average of 100 measurements. The narrow linewidth despite reduced averaging at low fields is a promising aspect of the technique. Figure courtesy of McDermott et al. [4]

involves using a ulf-MRI system for airport security, which suggests that there may be more unclaimed areas where this technology can be beneficial [8].

1.2 Future outlook

For our group, the ultimate system would be able to perform both Magnetoencephalography-measurements (MEG) and MRI-measurements in the same setup.

MEG is a method of measuring brain activity by using SQUID detectors. Then one can directly measure the magnetic field arising from neural activity which has many benefits when compared to other neuroimaging technologies. For example, the advantages of using MEG over EEG is that it is easier to calculate the signal source location, since the magnetic field is less affected by the electric properties of the different tissues in the brain compared to the electric field. MEG is also faster than functional MRI, since you measure the magnetic fields directly whereas functional MRI measures the difference in blood flow in the brain.

The localization algorithms in MEG benefit from having patient-specific structural information about the brain, which makes the visualization of the results more precise. It is possible to use images from high-field MRI for this task, but differences between the measurement systems might still affect the results. For example, if the patient is lying down during the MRI scan, the brain is slightly deformed and shifted compared to sitting up during MEG. When combining MRI and MEG in a single system, the localization algorithms would benefit from a combined semi-simultaneous structural and functional information about the brain from one and the same system [9].

2 Theory, NMR and MRI

In NMR the nuclear spin energy levels are split when they are exposed to an external magnetic field, similar to the Zeeman effect for electrons. In our work, we are concentrating on the hydrogen nuclei in water, since they achieve a high magnetization, and are abundant in biological materials, which will later be used in MRI.

When the spins are exposed to an external field perpendicular to their magnetic moment, they start precessing around the field vector with the Larmor frequency. In the following section, we will mostly use the classical derivations since they work sufficiently well and provide an easy understanding of the principles.

2.1 Magnetization

When the nucleus is exposed to an external magnetic field, $\mathbf{B}$, the energy levels for the different spin states are split. The angular momenta can either orient themselves parallel- or antiparallel with respect to the external field. Since the hydrogen nuclei have spin $I = \frac{1}{2}$, we simply get a two-level system with quantum numbers $m = \pm\frac{1}{2}$.

We can then use that the dipolar magnetic moment, $\boldsymbol{\mu}$, is $\mu = \gamma\hbar m$, $\forall m \epsilon [-I...I]$, where $\hbar$ is Planck's constant divided by 2π. We arrive at the following expression for the splitting of the energy levels:

$$E = -\boldsymbol{\mu} \cdot \mathbf{B} \Rightarrow E_m = -\gamma\hbar m B \tag{1}$$

This means that each nucleus has 2 energy levels to choose from. In order to calculate the net magnetization we use a Boltzmann distribution for the energy levels at room temperature:

$$M = N\gamma\hbar \frac{\sum_{-I}^{I} m \exp(\gamma\hbar m B/kT)}{\sum_{-I}^{I} \exp(\gamma\hbar m B/kT)} = \frac{N\gamma\hbar}{2} \frac{e^{\frac{\gamma\hbar B}{2kT}} - e^{-\frac{\gamma\hbar B}{2kT}}}{e^{\frac{\gamma\hbar B}{2kT}} + e^{-\frac{\gamma\hbar B}{2kT}}} = \frac{N\gamma\hbar}{2} \tanh(\frac{\gamma\hbar B}{2kT}) \tag{2}$$

where N is the number of atoms [10].

For water, $\gamma = 267.513 \times 10^6$ rad/(s T), which means that the net magnetization from the hydrogen atoms in water is $3.2058 * \times 10^{-3}$ Am^2 per m^3 of water and applied Tesla. This will later be used in the simulations in section 4.3.1.

2.2 Larmor frequency

In the classical picture, the spin vector experiences torque in the direction $\boldsymbol{\mu} \times \mathbf{B}$ when exposed to an external magnetic field $\mathbf{B}$. Since torque is the rate of change of angular momentum, we get the following:

$$\frac{d\boldsymbol{\mu}}{dt} = \boldsymbol{\mu} \times \gamma\mathbf{B} \tag{3}$$

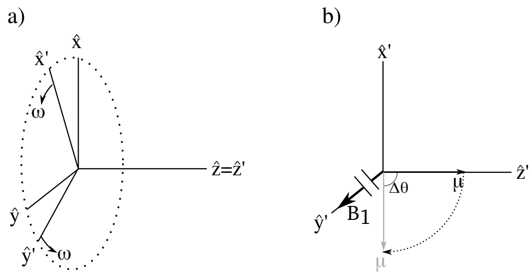

Figure 2: a) The rotating frame compared to stationary. b) The oscillating external field $\mathbf{B_1}$ rotates the nuclear magnetic moment in the rotating frame.

This describes a simple rotation around the $\mathbf{B}$ vector, so if we solve the equation, we find that the spin precesses around the $\mathbf{B}$ axis with an angular velocity of $\omega = -\gamma B$ [11, p. 13]. We can also note that $\hbar\omega = \hbar\gamma B$ is the magnitude of the energy level splitting in the applied field, discussed in section 2.1.

2.3 Excitation pulse

When using a static $\mathbf{B_0}$-field, the spins relax to an equilibrium alignment parallel or antiparallel to the field, which means that the rotation is impossible to detect. To fix this, we have to tip the spins into the xy-plane, so that the rotation is measurable. This is done with an excitation pulse, which is where we apply a small oscillating field for a short period of time. We will see that the tipping angle depends on the strength of the oscillating field and for how long it is applied. The maximum signal is achieved when the angle is $\frac{\pi}{2}$ radians, which leads to the naming of the corresponding excitation pulse as a $\frac{\pi}{2}$-pulse.

First we need to introduce the rotating frame, which is simply a rotating coordinate system, compared to the Cartesian laboratory frame, see figure 2.a.

When we want to convert fields from cartesian coordinates to the rotating frame we can project the vectors onto each other according to equation 4.

$$\begin{cases} \hat{\mathbf{x}} = \hat{\mathbf{x}}' \cos(\omega t) - \hat{\mathbf{y}}' \sin(\omega t) \\ \hat{\mathbf{y}} = -\hat{\mathbf{x}}' \sin(\omega t) + \hat{\mathbf{y}}' \cos(\omega t) \\ \hat{\mathbf{z}} = \hat{\mathbf{z}}' \end{cases} \tag{4}$$

When using a resonant excitation field, $\mathbf{B_1}$, we apply an oscillating pulse with the Larmor frequency, ω_0, in the $\hat{\mathbf{y}}$ direction, which becomes a simple expression in the rotating frame (also using the Larmor frequency).

$$\mathbf{B_1} = B_1 \cos(\omega_0 t)\hat{\mathbf{y}} \tag{5}$$

$$= -B_1 \cos(\omega_0 t)\sin(\omega_0 t)\hat{\mathbf{x}}' + B_1 \cos(\omega_0 t)\cos(\omega_0 t)\hat{\mathbf{y}}' \tag{6}$$

$$= -\frac{B_1}{2}\sin(2\omega_0 t)\hat{\mathbf{x}}' + \frac{B_1}{2}(1+\cos(2\omega_0 t))\hat{\mathbf{y}}' \tag{7}$$

If we assume that our excitation pulse is long compared to the period of the oscillations, the effect from terms oscillating at twice the Larmor frequency average out. We can simplify this to

$$\mathbf{B_1} \approx \frac{B_1}{2}\hat{\mathbf{y}}' \tag{8}$$

We get a new expression for the equation of motion:

$$\frac{d\boldsymbol{\mu}}{dt} = \frac{\gamma B_1}{2}\boldsymbol{\mu} \times \hat{\mathbf{y}}' \tag{9}$$

Since $\boldsymbol{\mu}$ and $\hat{\mathbf{y}}'$ are perpendicular, this simply describes a rotation around the $\hat{\mathbf{y}}'$-axis. The expression for the rotation, $\Delta\theta$, as a function of excitation time, τ, becomes [12]:

$$\Delta\theta = \frac{\gamma B_1}{2}\tau \tag{10}$$

2.4 Relaxation times, T_1 and T_2

So far we have only looked at free protons, not interacting with each other. When adding the interactions, we instead have to look at the combined effect from an ensemble of spins. This becomes significally more complicated, but we can safely assume that the system will try to find an equilibrium, which can be achieved by exchanging energy with each other and the environment.

F. Bloch [13] introduced material-specific phenomenological time constants, T_1 and T_2, to be able to describe this process. We divide the magnetization into two components, M_z and M_{xy}. M_z is parallel to the external field, and M_{xy} is perpendicular. Bloch was then able to describe the magnetization of the components by an equation similar to exponential decay [11].

2.4.1 T_1, Spin-lattice relaxation

The T_1 parameter describes how the magnetization relaxes in the direction parallel to the external field:

$$M_z(t) = M_z(0)e^{-t/T_1} + M_0(1 - e^{-t/T_1}) \tag{11}$$

$M_z(0)$ is the starting value and M_0 is the equilibrium value of the magnetization.

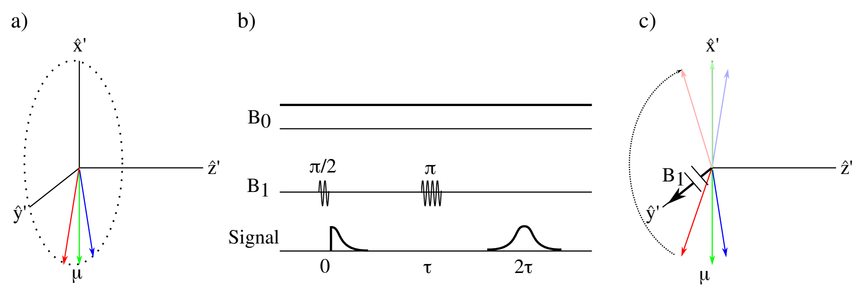

Figure 3: a) A short time after the $\frac{\pi}{2}$-pulse. The colors identify a spin at a certain frequency, and we see that they have fanned out. b) A spin echo pulse seqence. c) The π-pulse rotates the spins π radians along the $\hat{\mathbf{y}}$-axis. If the dephasing is caused by field inhomogeneity, this means that the faster moving spins (red) are now behind the slower ones and will catch up. Figure reconstructed from Slichter [11].

In NMR this is useful to see how long we need to prepolarize the sample to get the largest magnetization. The expression also determines how long it takes after a spin-flip until we can run another excitation.

2.4.2 T_2, Spin-spin relaxation

The spin-spin interaction in the rotating xy-plane makes the spins dephase. In the rotating frame this can be viewed as if the spins are fanning out, see figure 3a. Since the vectors cancel each other out, the total magnetization in the xy-plane decreases.

$$M_{xy}(t) = M_{xy}(0)e^{-\frac{t}{T_2}} \tag{12}$$

T_2 is our most important parameter, since it determines how long we can acquire a signal after a $\frac{\pi}{2}$-pulse [12, p. 54].

The spin-spin interactions are not the only cause for dephasing. If the magnetic field deviates ΔB over the sample volume, the different parts will spin with a slightly different frequency, $\Delta f = \frac{\gamma \Delta B}{2\pi}$. When considering the total dephasing effect, T_2^*, we want to separate the extrinsic dephasing caused by our experimental setup, $T_2' = \frac{1}{\Delta f}$, from the intrinsic parameter, T_2. In our calculations, we use the following expression for the total dephasing effect:

$$\frac{1}{T_2^*} = \frac{1}{T_2} + \frac{1}{T_2'} \tag{13}$$

We can compensate for the extrinsic dephasing by applying a π-pulse, discussed next.

2.5 Spin-echo

E. Hahn [14] discovered that there is a simple way to work around experimental dephasing , T_2', by applying a π-pulse at time τ. Then you are able to detect a large signal at time 2τ, an echo. This is quite easy to explain when looking at the dephasing of the spins caused by the inhomogeniety of the measurement field.

Figure 3.b describes the pulse sequence for spin-echo. The principle behind the π-pulse is the same as for the $\frac{\pi}{2}$-pulse, but we rotate the spins π radians instead, see figure 3.c. If the spins are flipped at time τ, the spins at the slightly higher frequency will be now be behind, but will eventually catch up. This means that the signal will grow stronger and at time 2τ the spins will be in phase again, which means that the signal reaches its local maximum. Note that the intrinsic dephasing can not be rectified with this method [11].

2.6 Pulsing sequences

In order to get any signal, we want the spins to precess around the measurement field, $\mathbf{B_0}$, with the Larmor frequency. Since the spins are mostly aligned parallell or anti-parallell to $\mathbf{B_0}$, we have to activate them. There are quite a few different pulsing sequences, and some groups (for example McDermott et al. [4], [18]) have switched sequence during their progress, so we need to choose one that fits our measurement system.

An important factor when choosing a particular sequence is if the turn-off of the prepolarizing pulse is adiabatic or non-adiabatic. If it is adiabatic, the polarization will follow the resulting field direction during the turn-off, and align with $\mathbf{B_0}$. On the other hand, with a non-adiabatic turn-off the prepolarization field is decreased too quickly for the polarization to follow, and it will instead start rotating around $\mathbf{B_0}$.

Melton et al. [15] have suggested the following condition for non-adiabatic turn-off:

$$\left|\frac{dB_p}{dt}\right| \gg \gamma B_0^2 \tag{14}$$

where γ is the proton gyromagnetic ratio.

Other research groups do the approximation that the turn-off can be regarded as non-adiabatic if it takes less time than the period of the Larmor frequency [17].

Free induction decay The simplest method, proposed by Qiu et al. [16], is to apply a polarizing pulse in a direction perpendicular to $\mathbf{B_0}$. If you turn off the pulse non-adiabatically, the magnetic spins end up perpendicular to $\mathbf{B_0}$ and will then rotate at the Larmor frequency while slowly (order of seconds $\sim T_1$) aligning to $\mathbf{B_0}$.

The upside of this approach is that you only need 2 coils, and the pulsing programming is easy to implement, but it only works when $\mathbf{B_p}$ is ramped down non-adiabatically. See figure 4.a.

Turning on $\mathbf{B_0}$ Zotev et al. [17] needed a scheme where they could ramp down $\mathbf{B_p}$ adiabatically. Then, they first apply only $\mathbf{B_p}$, which is ramped down, but the magnetization is still in the $\hat{\mathbf{y}}$-direction, since this is the only field that has been present. When $\mathbf{B_0}$ is ramped up, the spins start rotating. See figure 4.b. The upside of this approach is that you can use coils with higher inductance, while the downside is that you lose some of the signal during the ramps.

Excitation pulse scheme McDermott et al. [18] proposes yet a different approach, inspired by the principles in high-field NMR. They ramp down the $\mathbf{B_p}$ pulse adiabatically, while $\mathbf{B_0}$ is turned on. This means that the spins turn their alignment along $\mathbf{B_0}$ instead. Then they apply an excitation, $\frac{\pi}{2}$-pulse, which gradually flips the spins, as described in section 2.3.

The upside of this method is that you can keep $\mathbf{B_0}$ constant, and $\mathbf{B_p}$ can be ramped down adiabatically. The downside is that you need an extra coil, and the configuration of the excitation pulse is harder to implement. See figure 4.c.

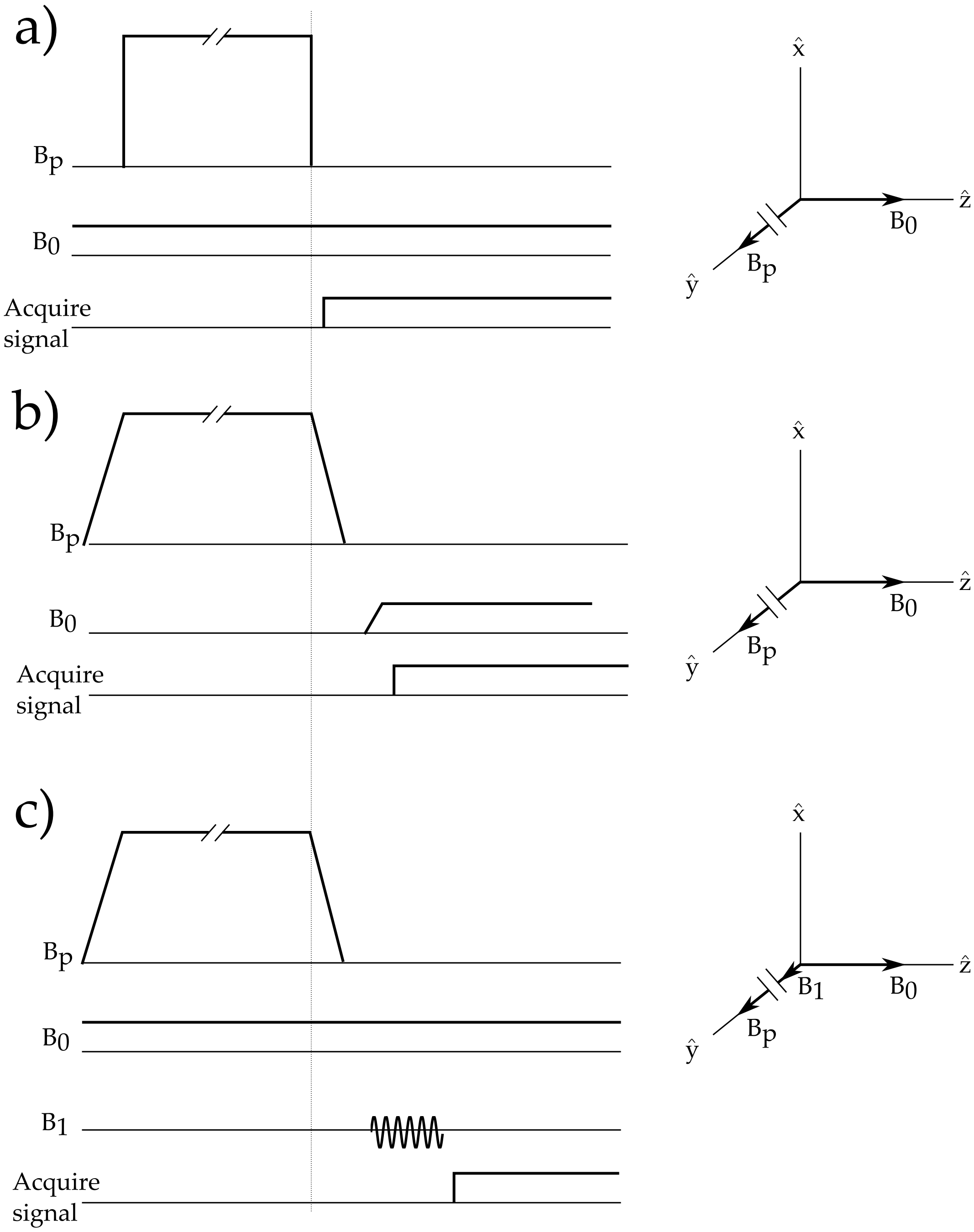

Figure 4: a) Pulse sequence with non-adiabatic turnoff for $\mathbf{B_p}$. b) Sequence for adiabatic turnoff of $\mathbf{B_p}$ and adiabatic turn-on of $\mathbf{B_0}$. c) Sequence for adiabatic turnoff of $\mathbf{B_p}$ and usage of excitation pulse. Figure reproduced from Qiu et al. [16], Zotev et al. [17] and McDermott et al. [18]

.

2.7 MRI

In Magnetic Resonance Imaging we use the principles of NMR to construct images of the soft tissue. In short, this can be done by applying a non-uniform field over the sample, resulting in a variation of the Larmor frequency in each region of the sample. By analyzing the frequency spectrum of the signal, we are able to extract spatial information about the distribution of hydrogen nuclei.

2.7.1 1D Imaging

To get spatial information in one dimension, we need to apply a gradient field, G. When considering coil design, we find that the easiest direction to apply this gradient is along the $\hat{\mathbf{z}}$-axis, where we can use the well-known Maxwell pair. Pascone et al. [19] states that two counter-wound coils with radius r spaced apart at distance $1.73r$, gives us a uniform gradient, G_z. The resulting field depends linearly on the position along the $\hat{\mathbf{z}}$-axis.

$$B(z) = B_0 + zG_z \tag{15}$$

Since the Larmor frequency is proportional to the applied field, we can get spatial information of the sample by investigating the frequency spectrum. This is also why G_z sometimes is called the frequency encoding gradient.

2.7.2 2D Imaging

In order to construct an image in more dimensions, we need to apply more gradients. By adding a gradient in the $\hat{\mathbf{y}}$-direction, G_y, we get two parameters to control. Note that the field is always directed in the $\hat{\mathbf{z}}$-direction, only the magnitude changes with position.

$$B(y, z) = B_0 + yG_y + zG_z \tag{16}$$

In our experiments we use filtered backprojection to construct our image, which is a method similar to the ones used in Computer Assisted Tomography (CAT-scans). By changing G_y and G_z we can rotate the gradient vector, which means that we can collect cross-sections of the sample in different directions. The cross-sections are then projected along each angle and combined into a single image, in our case with the help of the MATLAB function `iradon`. Since backprojection uses a polar representation that we convert into a rectangular grid, this method can introduce artifacts into the image, which Gonzales & Woods [20] discuss in more detail. They also demonstrate that the method introduces some blurring of the image, which means that the difference between 32 and 64 projections is very small when not using further image processing.

2.7.3 3D imaging

Backprojection is quite tedious to perform in 3D space, so other methods have been developed. One of them is called phase-encoding, where G_z is kept constant, but G_x and G_y are only applied during a short period of time. This induces a position-dependent phase difference in the spin rotation, which can be extracted when performing the Fourier transformation of the signal. 2D imaging can also be performed with this method by just using one gradient, but since the method includes pulsing of the fields the experimental setup is more complicated than for backprojection. For further information about phase encoding, I recommend reading Clarke et al. [1].

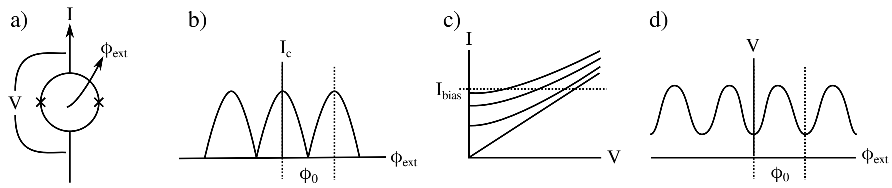

Figure 5: a) Principle of SQUID b) I_c dependence of flux Φ c) I-V curve at different Φ d) V-Φ curve at constant bias current. Image reconstructed from J.R. Waldram [21, p. 348]

.

3 Theory, SQUID

One of the reasons that ultra-low field MRI has a chance to be successful is the use of a different kind of detector for measuring the magnetic signal. A Superconducting Quantum Interference Device (SQUID) magnetometer can be used to measure the magnetic field directly. A main advantage of this detector is that the sensitivity can be made essentially constant from 1 Hz to 10kHz, or higher. Since the Larmor frequency is directly related to field strength, this means that we are able to do measurements at fields as low as μT. Myers et al. [22] calculated that the signal-to-noise-ratio (SNR) in MRI detection using a SQUID is better than that of a faraday detector at fields lower than 250 mT, but this is dependent on the geometry of the sensor.

3.1 SQUID basics

A SQUID consists of a superconducting loop, containing two junctions (Josephson junctions), see figure 5.a. The junctions give rise to the Josephson effect, giving a phase shift in the superconducting current. The flux through the superconducting ring also sets a requirement on the phase difference, and together they form an interference pattern for the critical current similar to Youngs double slit, see figure 5.b. This is exhaustively reviewed by J.R. Waldram [21, p. 104].

Since the critical current changes with the magnetic flux through the SQUID, the I-V curve of the SQUID will also change accordingly, which can be seen in figure 5.c.

If we lock the bias current at a certain value, I_{bias}, and instead measure the voltage over the SQUID, we get a sinusoidal response to the applied flux, see figure 5.d.

3.2 Flux-locked loop, FLL

Since a linear change in the magnetic field causes a sinusoidal change in voltage over the SQUID, the SQUID is hard to use as a magnetometer out of the box.

We want to linearize the field response from the SQUID, which is achieved by feeding back the signal through a feedback coil. You choose a working point, where the response from the SQUID is at its steepest. By using a negative feedback of the SQUID output through the feedback coil, we can counteract the flux through the SQUID, and the SQUID is always around its optimal working point. Since the output is always corrected back to zero it is now not useful to read out the flux. By instead integrating the output signal we get the total change in flux, and since the signal is moving with small variations through the working point, the result will be linear [21, p. 354].

This process is handled by commercially available electronics in our setup (Magnicon [23]).

3.3 High temperature superconductor

For our SQUIDs we use a high-T_c superconductor, $YBa_2Cu_3O_{7-x}$. Since the SQUID then becomes superconducting at 89K, we are able to use liquid nitrogen to cool it. This has a lot of advantages such as fast cooling times in experiments, and cheaper setup compared to low-T_c superconductors.

The problem with using SQUIDs of this material is that the noise levels are higher, which is partly caused by the higher temperature. Another obstacle is that the material is not flexible, so it is hard to make superconducting wires or axial gradiometers. The cause of the superconductivity in this material is also not completely understood.

3.4 SQUID noise

SQUIDs have a dominant source for noise at lower frequencies, called *1/f* noise. There are two probable causes for this:

- Trapped flux vortices in the film experiencing thermal motion, affecting the total flux through the SQUID.
- Fluctuations in the critical current of the Josephson junctions.

It has been shown that during normal operation, the dominant cause of noise in high-T_c SQUIDs is fluctuations in the critical current [24].

The solution is simple; by switching the sign of the bias current with a high frequency (100 kHz), you are able to even out the fluctuations in the output voltage. This is commonly called AC-mode [23].

This method is very important in MEG which deals with low-frequency signals, but in NMR the expected signal has a frequency of 3.5 kHz. From figure 6 in section 4.1.2 we can see that the mode is arbitrary at this higher frequency since white noise becomes a dominant factor instead.

4 Understanding the measurement environment and our sensors

It was necessary to perform some tests and simulations of our measurement setup to get an idea of how large signal we can expect and if we are able to detect it. In these investigations some peculiarities have arisen, which are discussed in this section.

4.1 SQUID investigations

4.1.1 SQUID setup

We have tried two different SQUID configurations for our NMR and MRI experiments.

For our first experiments, we were using a high-T_c SQUID in a gradiometer configuration, which is made in-house. In order to get as close to the sample as possible, we were using a low-noise glassfiber cryostat (ILK Dresden), where the SQUID is kept in vacuum but connected to a liquid nitrogen bath through a sapphire rod cooling the SQUID. It was possible to move the SQUID close to a sapphire window, which means that the distance between the sample and the SQUID could be decreased to below 1 mm. We based our simulations on this setup, which can be found in section 4.3.

In section 2.7 we saw that we need to prepolarize the sample in a high magnetic field ($\sim$20 mT) before performing the measurements. Since the SQUID is placed near the sample it experiences roughly the same field. We tried to minimize the effects of this by placing the SQUID plane perpendicular to the magnetic field, but it still proved to be causing our SQUID to unlock, trap flux or just behave inconsistently. This is the reason why we instead tried using a SQUID magnetometer inside a superconducting shield, see section 5.1.4.

In both cases, we use the Magnicon SEL-1 SQUID electronics to control the bias current and keep the SQUID in a flux-locked loop.

4.1.2 Noise levels of SQUID

We used a SR780 Dynamic signal analyzer (Stanford Research Systems Inc.) to investigate the noise characteristics of the SQUID gradiometer. In figure 6 we see that the noise level is less than 20 $\mu\Phi_0/\sqrt{\mathrm{Hz}}$ RMS in AC-mode. At our expected Larmor frequency of 3.5 kHz, the bias mode does not seem to matter. The noise levels of our shielded SQUID magnetometer are comparable.

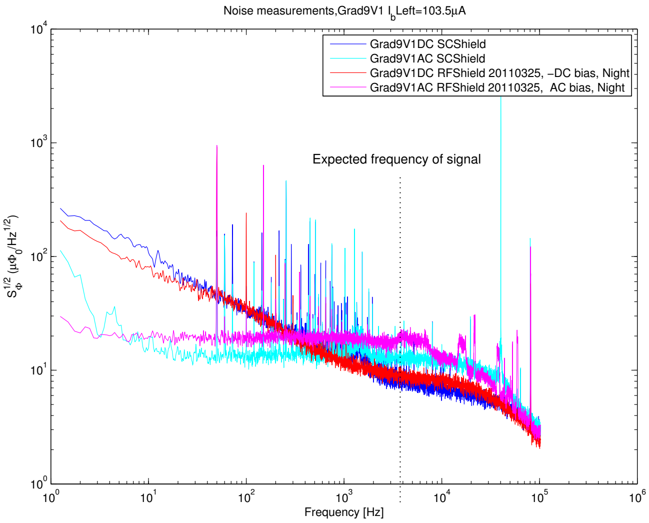

Figure 6: Comparison of noise measurements for the SQUID in superconducting shield and in RF-shielded room.

4.1.3 SQUID layout

In figure 7 we see the actual SQUID gradiometer layout. The SQUID chip was constructed and manufactured by Fredrik Öisjöen and is described in detail in his thesis [31]. It consists of two loops connected into a planar gradiometer, which couples flux into two hairpin SQUIDs. Only one of the SQUIDs is used, the other is incorporated for redundancy.

4.2 SQUID gradiometer balance

Since we experienced some difficulties keeping the unshielded SQUID operable after pulsing high fields, we wanted to investigate the balance of the SQUID gradiometer. We placed the SQUID so that the magnetic field would be directed vertically into the gradiometer plane. We then applied a field in the form of a slow moving triangular wave, and recorded the output from the SQUID. This lead to some unexpected discoveries, which can be seen in figure 8.

If we first look at the magenta curve, we see that the response from the unlocked SQUID starts as expected, with a long sinusoidal shape. When the applied magnetic field reaches 0.75 μT the behaviour switches, and we instead get a quickly oscillating signal, which suggests that the SQUID has become significantly more sensitive to the magnetic field. When the field direction switches, the behaviour suddenly becomes normal again, only to switch after a short while. When moving at half the pace, the switches occur at the same field strengths, so there does not seem to be a time dependence.

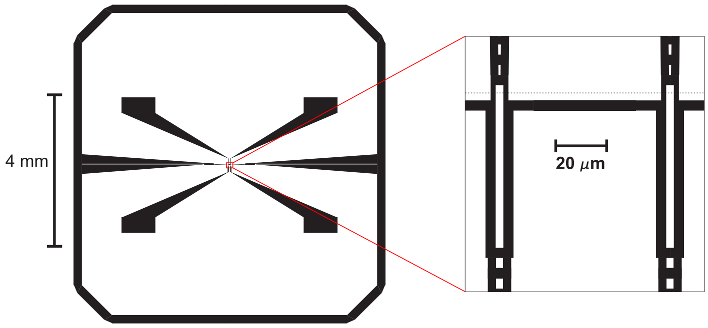

Figure 7: Our SQUID gradiometer layout. The two hairpin SQUIDs are magnified.

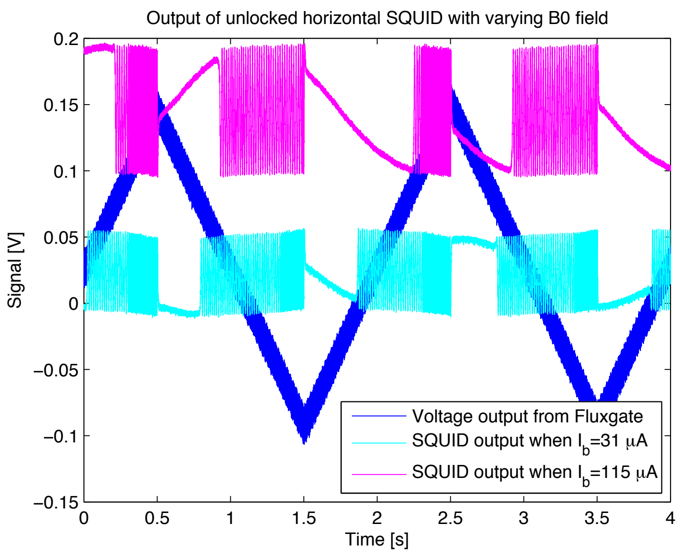

Figure 8: Output from the unlocked SQUID at two different temperatures (exact values unknown), resulting in two different optimal bias currents. 0.1 Volt output from the fluxgate corresponds to a field strength of 1 μT.

The cyan curve describes the behaviour of the same SQUID kept at a slightly higher temperature, resulting in a lower critical current. We see that the curve switches at a lower field, which seems to suggest that there is a temperature dependence. An explanation to the phenomenon can be that there are flux dams (20 Josephson-junctions in parallel) incorporated into the design, which are expected to turn normal when the current is too high, thereby protecting the SQUID. If one of the pick-up loops in the gradiometer becomes normal before the other loop, it would mean that the SQUID suddenly is converted to a magnetometer and becomes more sensitive. On the other hand, this does not explain the behaviour when switching field direction. We judged that it was outside the scope of this thesis to find the solution to this problem, so it remains as an obstacle to be solved.

4.3 Simulations

We have performed simulations for the expected signal for two different designs of the prepolarization coil, but in both cases we expect a gradiometer SQUID to be placed relatively close to the sample (within 2 cm).

Configuration 1: In the first case, we use a large Helmholtz coil pair, with the head of the cryostat placed between the coils at the center of the applied field. The sample is placed directly on top of the cryostat window. As discussed before, we experienced serious problems with keeping the SQUID locked after the prepolarization pulse with this coil design.

Configuration 2: We concluded that a better way would be to avoid placing the SQUID directly in the middle of the field, so in the second case we instead use a smaller solenoid coil. The sample is placed inside the coil, whereas the SQUID is placed outside. This is illustrated by the sample discretization and SQUID layout in figure 9.

All coils used in our experiments are described more thoroughly in section 5.1.2.

4.3.1 Signal from prepolarized sample

We want to estimate how large signal we can expect from a water sample. From section 2.1 we know that the magnetization of water is 3.2058×10^{-3} Am^2 per applied Tesla and m^3 of sample.

We also use that the magnetic flux density in position $\mathbf{r}$ generated by a magnetic dipole placed at the origin (0,0,0) is:

$$\mathbf{B}(\mathbf{r}) = \frac{\mu_0}{4\pi}\left(\frac{3(\mathbf{M}\cdot\mathbf{r})\mathbf{r}}{r^5} - \frac{\mathbf{M}}{r^3}\right) \tag{17}$$

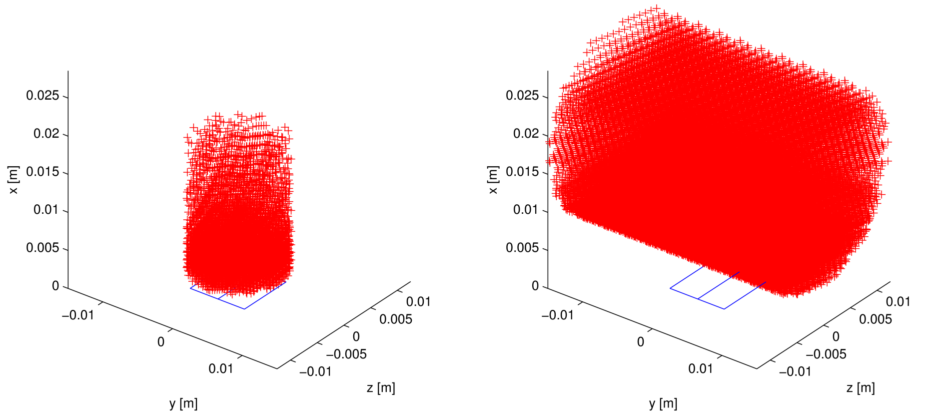

Figure 9: **Configuration 1:** The left figure describes the discretization of a cylindrical sample volume, r=6 mm V=2.5 ml. Note that only 1/30th of the samples are plotted. Since the magnetic field decreases with the distance cubed, the points furthest from the gradiometer can be spaced at longer intervals in order to cut down computation time. **Configuration 2:** The right figure describes the discretization of a sample inside a solenoid coil. Note that only 1/30th of the samples are plotted.

where **M** is the magnetization vector of the dipole [26].

Depending on which prepolarization coil is used, we have two different sample volumes to work with.

Configuration 1, Cylindrical sample near SQUID When using a large Helmholtz prepolarization coil, we can use vials with a base radius of 6 mm, placed directly on top of the SQUID.

Since the sample is close to the SQUID, we cannot approximate it with a single dipole. We discretize the sample volume into a lot of smaller volumes, each of them approximated as a small dipole. We can then add up all the small contributions, and calculate the combined flux through the gradiometer. Figure 9 describes the discretization of a 2.5 ml water sample placed in the optimal position 2 mm above the gradiometer.

By moving the sample, we were also able to calculate the loss of signal when placing the sample in a sub-optimal position.

Configuration 2, Sample in solenoid prepolarization coil When using the solenoid prepolarization coil, the SQUID is placed outside the coil so the sample is located further away from it. The geometry of the sample is now instead a tilted cylinder, which is illustrated in the discretization on the right side of figure 10.

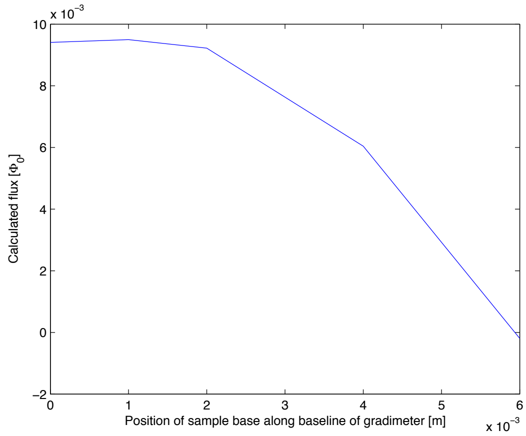

Figure 10: **Configuration 1:** Expected flux through the gradiometer for different positions of the cylindrical sample along the baseline. Bottom of sample placed 2 mm above SQUID. Sample: Radius=6 mm Volume=2.5 ml. 1 mT applied field.

4.3.2 Simulation results & Discussion

Configuration 1, Cylindrical sample near SQUID From the simulations we can conclude that the signal from the sample should be in the order of 10 mΦ_0 in 1 mT field. This should be more than sufficient for our measurement setup when compared to the noise levels of the SQUID in figure 6. When moving the sample in a sub-optimal position, I also found that the signal decreases, but is still within reasonable limits when the sample is moved less than 2 millimeters. We also have to consider the sensitivity of our data aquisition equipment. 10 mΦ_0 would give us a signal amplitude of 3.2 mV. This is well above the sensitivity of the equipment; 6μV [27].

Configuration 2, Sample in solenoid prepolarization coil The simulations of the solenoid sample indicates that the net flux in the gradiometer is 2.7 mΦ_0 in a 1 mT field, which is significantly smaller than for the Helmholtz coil. The reason that we still want to use a solenoid coil is that the SQUID will then be placed outside the magnetic field, which can lead to using a larger prepolarization field. When using a 10 mT field, the SQUID output signal should be comparable to the Helmholtz configuration.

Comparison to small coil experiment To compare these theoretical values to our real world system, we placed a small coil on top of the cryostat above one of the loops of the SQUID gradiometer, see figure 11. A small sinusoidal signal was then applied over the coil for 200 ms (the expected T_2 relaxation time of water), while the output from the SQUID was recorded.

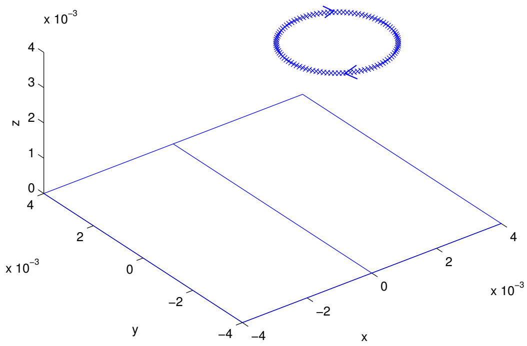

Figure 11: Coil placement on top of SQUID gradiometer.

The signal was transformed into a frequency spectrum with the help of a Fast Fourier Transform (FFT), which was averaged over 10 measurements. When lowering the amplitude of the sinusoidal signal, we were able to detect where the signal became indistinguishable from the noise in the FFT. By extrapolating the amplitude of the SQUID output signal, I deducted that the smallest detectable signal had an amplitude of 64 μV or 0.2 mΦ_0.

This looks promising at first sight, but when simulating the theoretical flux through the gradiometer from the coil, using the same coil-current as in the experiment, the theoretical SQUID output should be 20 mΦ_0.

Part of the explanation to this factor of 100 can be that the distance between the coil and the gradiometer is estimated to be 4 mm, but in reality this might differ at least a millimeter, which would halve the total flux. I also use a perfectly square geometry, and do not take into account the dynamics between the gradiometer pickup loops and the SQUID. One thing is at least certain, the signal will be a lot harder to detect with the SQUID gradiometer than first expected.

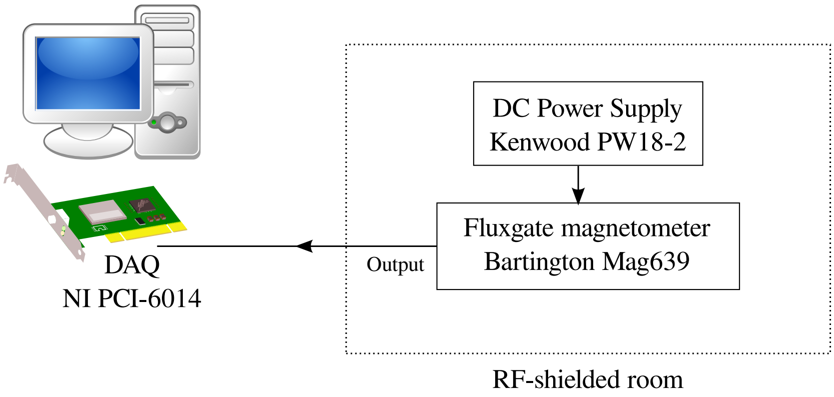

Figure 12: Experimental setup for measuring the long-time magnetic fluctuations.

4.4 Magnetic environment inside RF-shielded room

In our MRI-system we need to cancel the Earth's magnetic field, in order for us to control the magnitude and direction of the measurement field. A static cancellation is performed by coils fastened along the walls inside the shielded room (see section 5.1.2).

When tuning the cancellation fields we discovered that the magnetic field inside the shielded room still fluctuated with a magnitude in the order of 200 nT peak-to-peak with a period of seconds or even minutes. We wanted to investigate this further, so we did a longitudinal study of the magnetic field during a weekend and several weeknights.

4.4.1 Experimental details

We used the setup described in figure 12, where the output from our Mag639 fluxgate magnetometer (Bartington Instruments) was connected to the input of a NI PCI-6014 DAQ installed in a regular PC. The signal was measured in Labview at a samplerate of 1 kS/s for 72 hours. A 1 second moving average of the signal was then taken, before the result was downsampled to 100 S/s to save memory. The magnetic field was only measured in the vertical direction, since the fluctuations were largest in this axis, and due to problems with restricted memory in the PC.

4.4.2 Results & Discussion

The vertical external magnetic field in the shielded room is presented in figure 13. We see that the field fluctuates about 400 nT peak-to-peak during daytime, but is somewhat smaller after 03:00 on weekend nights. On weeknights, on the other hand, we can see a clear reduction in the fluctuations, down to 8 nT_{pp} between 02:35 and 03:35, which was confirmed by measurements during two other weeknights. This leads us to believe that the main cause might be the trams running beside and below the physics department.

According to e-mail correspondence with Dennis Sköldborg at Göteborgs Spårvägar AB, the trams require approximately 1800 A at 750 VDC. The rails function as the return line, so the lines are separated by 5 m. A quick calculation, using Biot-Savarts law, reveals that a 300 m power line segment at a distance of 100 m would contribute about 150 nT, which is in the order of the fluctuations we are experiencing.

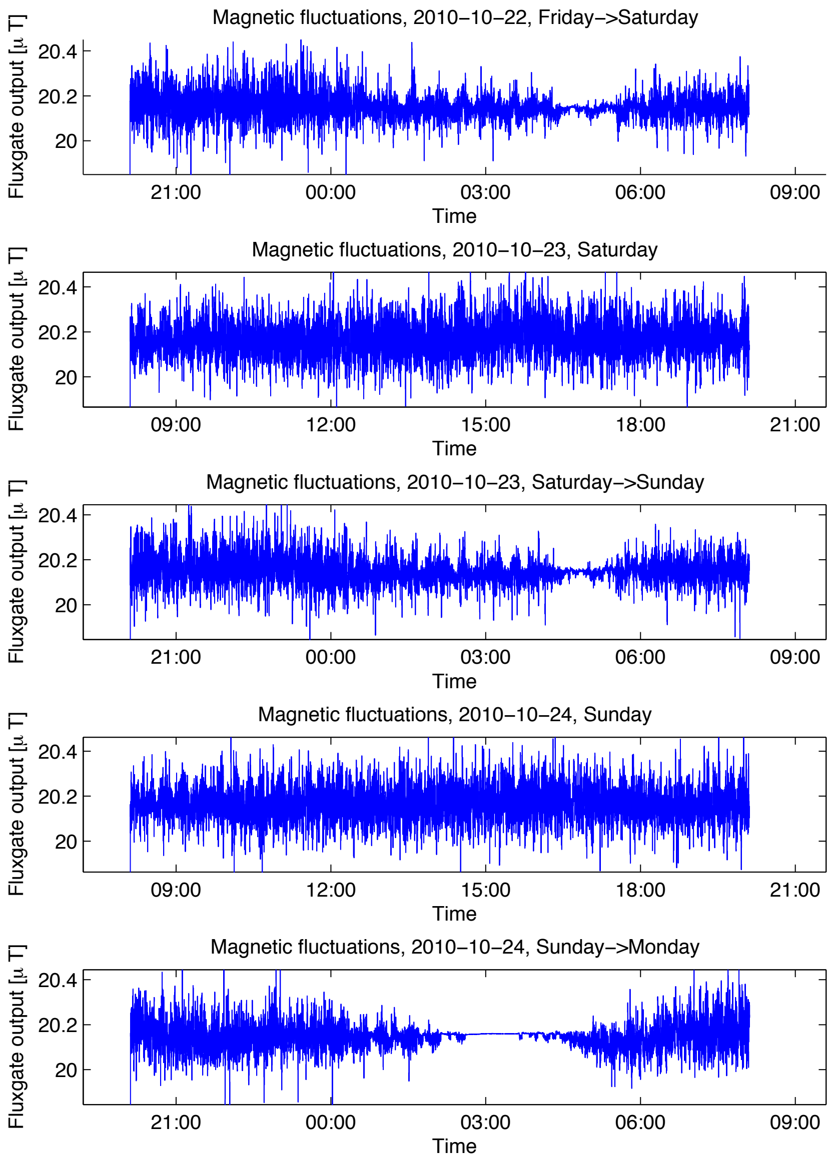

Figure 13: Fluctuations of the external magnetic field during a weekend, indicating the best time to measure is weeknights between 02:30 – 03:30 (bottom panel).

5 NMR and MRI

5.1 Experiment

We have used a few different experimental setups for our NMR and MRI measurements, so only the ones giving substantial results are described in this section. The main differences between the configurations are which prepolarization coil is used and the SQUID setup. We will start with a simple description of how we measured the coil inductances, followed by a detailed description of all the coils used. Then we will continue describing the whole measurement setup.

5.1.1 Inductance measurements

The inductance of a coil is an important parameter since it limits our ability to pulse a field through the coil quickly. For a Helmholtz coil, Javor & Anderson [28] has summarized the inductance calculations to the following expressions:

$$L_{total} = 2(L + M) \tag{18}$$

$$M = \alpha N^2 r \tag{19}$$

$$L = N^2 r \mu_0 \left[\ln\left(\frac{16r}{a}\right) - 2 \right] \tag{20}$$

where:
N=number of turns per coil
$\mu_0 = 4\pi \times 10^{-7}$ [H/m]
$\alpha = 0.494 \times 10^{-6}$ [H/m]
r =coil radius, [m]
a =diameter of wire bundle cross-section, [m]

When measuring the inductance, we used one of the methods described by S. Mak [29], where a known resistance, R, is connected in series with the coil that has a measured resistance r and unknown inductance L. We apply a sinusoidal signal with a frequency high enough so that the inductance becomes the dominant term in the impedance of the coil, $\omega L \gg r$. The known resistance is chosen so that $R \gg \omega L$, which means that the total impedance, Z, will be dominated by R. By measuring the voltage over coil, V_L, and the whole setup, V_Z, with an oscilloscope we can use simple voltage division to calculate the inductance of the coil:

$$\frac{V_L}{V_Z} \approx \frac{\omega L}{Z} \approx \frac{\omega L}{R} \Rightarrow L \approx \frac{V_L R}{V_Z \omega} \tag{21}$$

This is all described in detail by S. Mak [29].

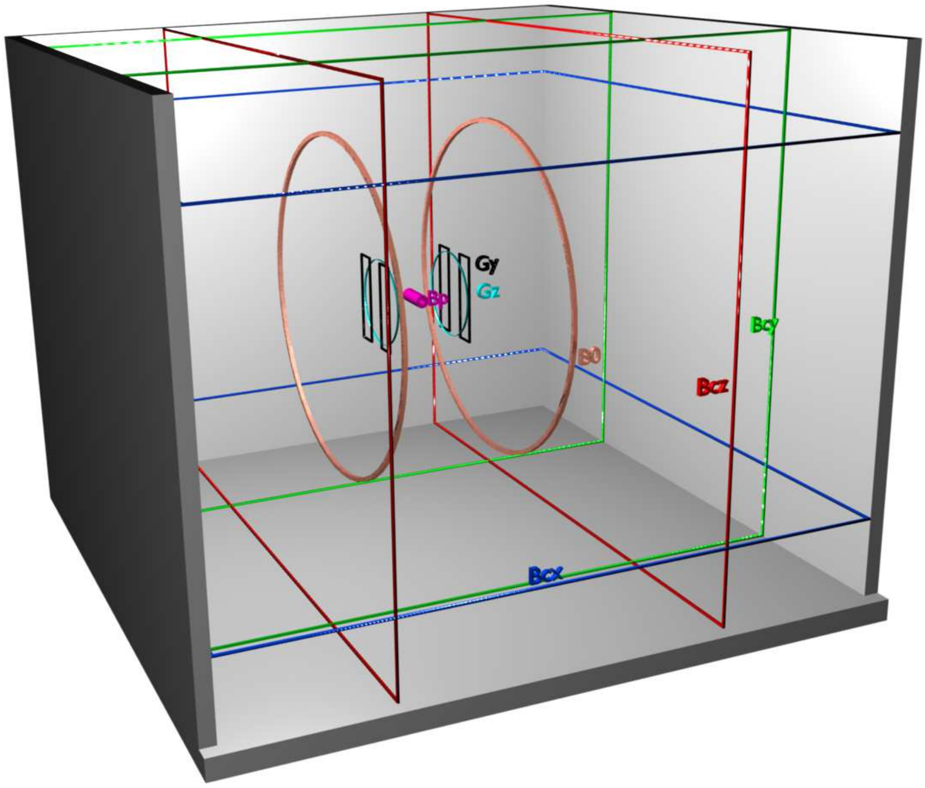

Figure 14: The coil setup for NMR and MRI. B_{cx}, B_{cy} and B_{cz} cancel Earth's magnetic field in all three directions. B_0 provides the measurement field and B_p produces the prepolarization field. G_y and G_z give us gradient fields for imaging. See table 1 for specifications of each coil.

5.1.2 Coil descriptions

Figure 14 contains a sketch of the different coils used for our NMR and MRI measurements, and figure 15 contains photo of the real setup. The coil characteristics can be found in table 1, but a more detailed description follows below.

Cancellation coils, $\mathbf{B_{cx}}$, $\mathbf{B_{cy}}$, $\mathbf{B_{cz}}$ For the cancellation of the earth magnetic field we use two rectangular coils, configured in a Helmholtz-like configuration, in each direction. Each coil is driven by a DC power supply, BK Precision 1745A. In order to get the coils out of the way, they are fastened along the walls of the room. COMSOL simulations showed that the optimal distance between the coils, giving the most homogenous field in the center of the room, is the average radius of the coils.

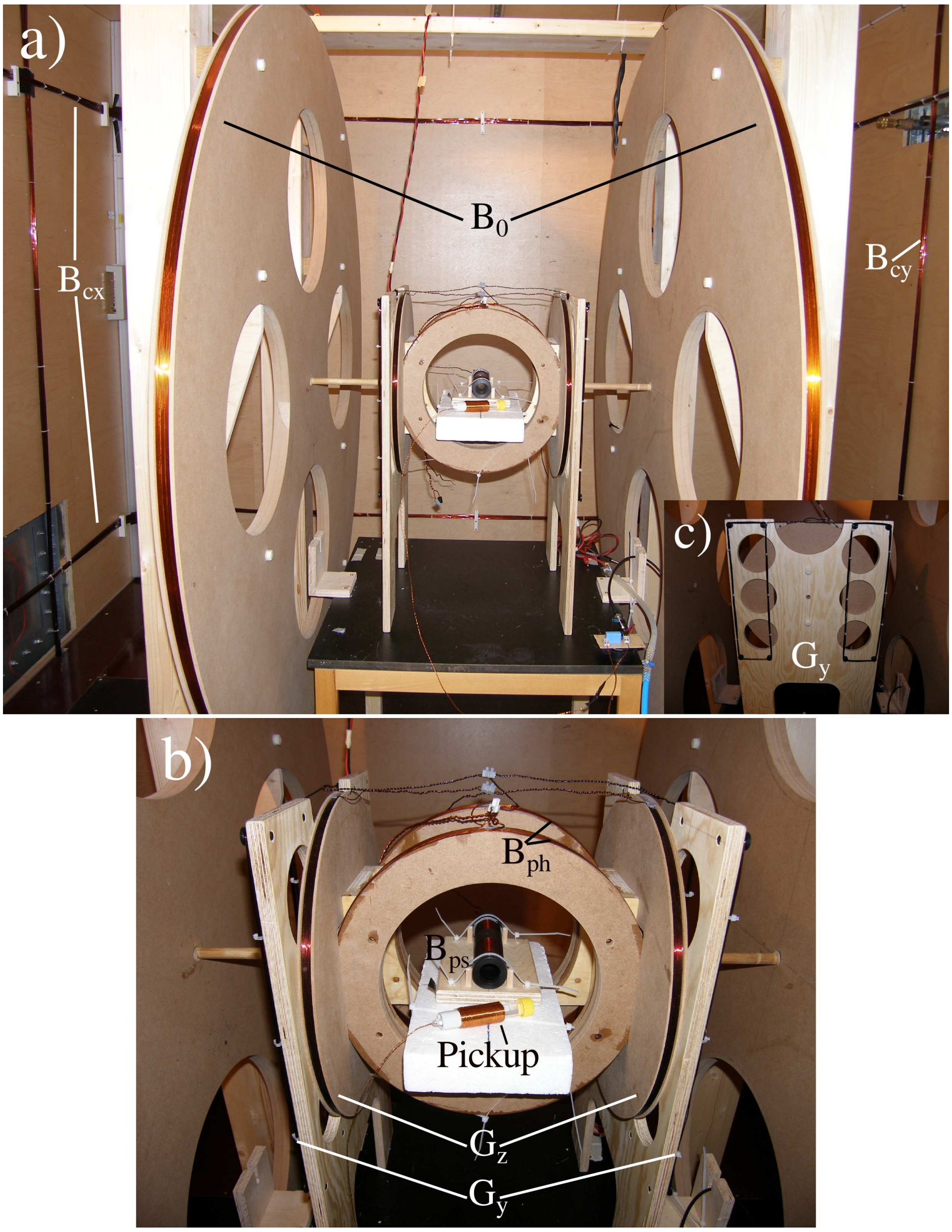

Figure 15: a) The final coil setup in the shielded room. We see part of the earth field cancellation coils B_{cx} and B_{cy} fastened along the walls. In the middle the measurement coil, B_0, dominates the view. b) A magnification of the smaller coil setup. In the middle we see the Helmholtz prepolarization coil, B_{ph}, and the smaller solenoid prepolarization coil, B_{ps}. The dimensions of the two gradient coils G_y and G_z were defined by the Helmholtz prepolarization coil. The pickup-coil is used in configuration 3 and is placed inside B_{ps}. c) Side shot of the G_y gradient coil.

Table 1: Coil characteristics.

Coil description	Field	Dimensions:	No of turns	Field strength	Inductance/Resistance Calculated	Measured
Cancellation coil, x-axis	$\mathbf{B_{cx}}$	2.93×2.93 m	20	10 μT/A	10 mH	6.2±0.5 mH 1.6 Ω
Cancellation coil, y-axis	$\mathbf{B_{cy}}$	2.93×2.37 m	20	10 μT/A	10 mH	5.7±0.5 mH 1.5 Ω
Cancellation coil, z-axis	$\mathbf{B_{cz}}$	2.93×2.37 m	20	10 μT/A	10 mH	5.9±0.5 mH 1.5 Ω
Measurement coil	$\mathbf{B_0}$	r=0.8 m	100	120 μT/A	80 mH	104±5 mH 10 Ω
Prepolarization coil, Helmholtz	$\mathbf{B_{ph}}$	r=0.165 m	95	1 mT/A	16 mH	50±5 mH 3.4 Ω
Prepolarization coil, Solenoid	$\mathbf{B_{ps}}$	Inner r=0.0127 m Outer r=0.020 m	450	4.5 mT/A	7 mH	1.0 Ω
Excitation coil	$\mathbf{B_1}$	r=0.027 m	10	3.4 μT/V @3.5 kHz	10 μH	
Gradient coil z-axis	$\mathbf{G_z}$	r=0.2 m	10	400 μT/(m·A)		1.1 Ω
Gradient coil y-axis	$\mathbf{G_y}$	0.1×0.4 m (w×h) Separation: 0.22 m	10	85 μT/(m·A)		0.9 Ω

Measurement coil, $\mathbf{B_0}$ The measurement field, B_0, is achieved by using two large coils in a Helmholtz configuration. We want these coils to be as large as possible, in order for our field to be as uniform as possible. This will be critical later when doing imaging over a larger sample volume. The current is supplied by a HP 6030A power supply.

Prepolarization coil, $\mathbf{B_{ph}}$ and $\mathbf{B_{ps}}$ We are using two different kinds of prepolarization coils. These are further described in section 5.1.3.

Excitation coil, $\mathbf{B_1}$ For the excitation field, we are using a fairly small coil (r=2.7 cm) in a Helmholtz configuration. It is driven by a Stanford DS345 synthesized function generator.

Gradient coils, $\mathbf{G_y}$ and $\mathbf{G_z}$ We have constructed a model system with two small gradient coils to test our MRI system. G_z is achieved with a Maxwell coil, as discussed in section 2.7. For the G_y gradient we use two biplanar coils, where the design has been optimized by Fredrik Öisjöen [31].

5.1.3 Prepolarization coils

As discussed in section 4.3, we have found that the prepolarization stage is the Achilles heal of our experiments, and is the biggest obstacle to overcome.

We want to use as high fields as possible to prepolarize the sample. Since we want to place the SQUID as close to the sample as possible, this means that the SQUID also will be subjected to the field. We try to minimize this effect by orienting the SQUID plane parallel to the field, which in theory would mean that no field penetrates the SQUID, but in reality we still have some flux coupling. This has lead us to using two different coil configurations, each of which has its own advantages. Our final approach was to avoid placing the SQUID in the magnetic field at all (configuration 3), see section 5.1.4 below.

Configuration 1: Helmholtz prepolarization coil, $\mathbf{B_{ph}}$ For our first experiments we used a large Helmholtz coil. The advantage of this approach is that the field is uniform, and that the configuration is open so that the SQUID can be placed near the sample. The disadvantage is that the inductance is higher, so we are not able to turn off the field non-adiabatically. This in turn means that an excitation coil is needed, and the pulse sequence becomes more complicated; see section 2.6. Another disadvantage is that the SQUID is placed directly in the magnetic field, which limits the strength of the prepolarization field.

Configuration 2: Solenoid prepolarization coil, $\mathbf{B_{ps}}$ By using a solenoid with 4 layers of wiring and a total of 450 turns, we are able to achieve a field strength of 4.5 mT/A. Since the SQUID is not placed directly in the magnetic field we are able to use a much higher field compared to the Helmholtz configuration. The drawback is that the sample is placed inside the solenoid, further away from the SQUID. The simulations in section 4.3.1 show that the higher field strength can make up for that.

In later experiments we have added a small loop connected in series with the prepolarization coil, and placed it near the SQUID. This cancelled the field through the SQUID further, and we were able to use a field strength of 9 mT.

In order to shut off the field non-adiabatically, we use *Clare CPC1918J* OptoMOS solid state relays to disconnect the coil from the amplifier. Each relay has a breakdown voltage of 120V, so 4 relays in series gives us 480V over the coil. This means that the pulse can be shut off in 150 μs. This process is further explained by Zotev et al. [17].

5.1.4 Configuration 3: Adding a copper transformer to the SQUID

When performing the experiment we soon found that even with the solenoid coil we still needed a way to shield the SQUID during the prepolarization pulse. The optimal way would be to construct a flux transformer using superconducting wire, which would mean that the SQUID can be placed inside a shield and be coupled inductively to the transformer. The drawback

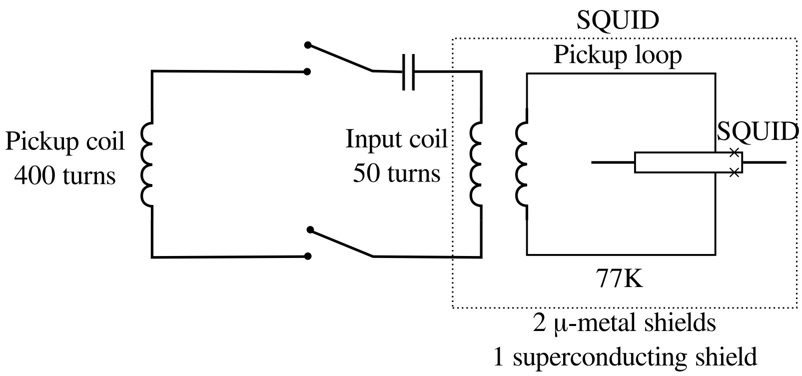

Figure 16: Schematic of the copper detection coil connected to the SQUID.

of using high-T_c SQUIDs is that although high-T_c superconducting wire is available, it is difficult to make superconducting joints, which means that constructing a superconducting wire flux transformer is not feasible for our project.

Liao et al. [30] has instead proposed using a copper flux transformer. This would mean that the SQUID can still be placed inside a superconducting shield, and a copper coil works as the detection coil.

The drawbacks are plentiful, such as the resistive losses in the copper wire, the fact that the signal strength now depends on dB/dt, and Johnson noise stemming from the wire resistance couples into the SQUID. The signal response can be improved by connecting a capacitor in series with the coils, thereby forming a resonant circuit. Figure 16 gives us an idea of the setup.

Simple theory of an LC-circuit show that the resonance frequency of the circuit can be found by $f_r = \frac{1}{2*\pi\sqrt{LC}}$, which means that the Larmor frequency of the sample can be matched by choosing a suitable capacitor. Liao et al. [30] showed that even with the losses in the pickup coil, they were able to achieve a single-shot SNR of 45 with 45 mT prepolarization.

We constructed a pickup coil that fits inside the solenoid B_ps, which consists of 400 turns of copper wire with a wire diameter of 0.7 mm. The coil has an inner diameter of 22 mm and a width of 75 mm. The total inductance of the coil is 0.7 mH, so when connecting 2.2 μF capacitor the theoretical resonant frequency becomes 4050 Hz. In reality the resonant freqency is 3810 Hz and the bandwidth of the coil is 700 Hz, which gives us a quality factor of 5.5. I believe that reducing the coil resistance, which currently is 1.25 Ω, would improve the quality factor significantly. The input coil consists of 50 turns of copper wire with a wire diameter of 0.35 mm and the diameter of the coil is 10 mm. A switch circuit has also been added to disconnect the pickup coil during the prepolarization pulse. The sample is placed inside the pickup coil and the pulse sequence stays the same as for the previous experiments, where we are using a non-adiabatic turn-off of the prepolarization field.

5.1.5 Connection schematics

A diagram of the connections are shown in figure 17. Our Labview program controls the pulsing sequence through the DAQ in the PC. Since the DAQ has a limited output current, we mostly use it for control pulses. The Fluke 282 arbitrary waveform generator generates the prepolarization pulse, which is amplified by the LVC5050 Power supply amplifier (AE Techron, Inc.). The other channel of the Fluke controls the pulse for the SQUID reset, which resets the integrator in the SQUID electronics, basically unlocking the SQUID during the prepolarization pulse. The output from the SQUID is connected to the DAQ analog input, and is recorded with the Labview program.

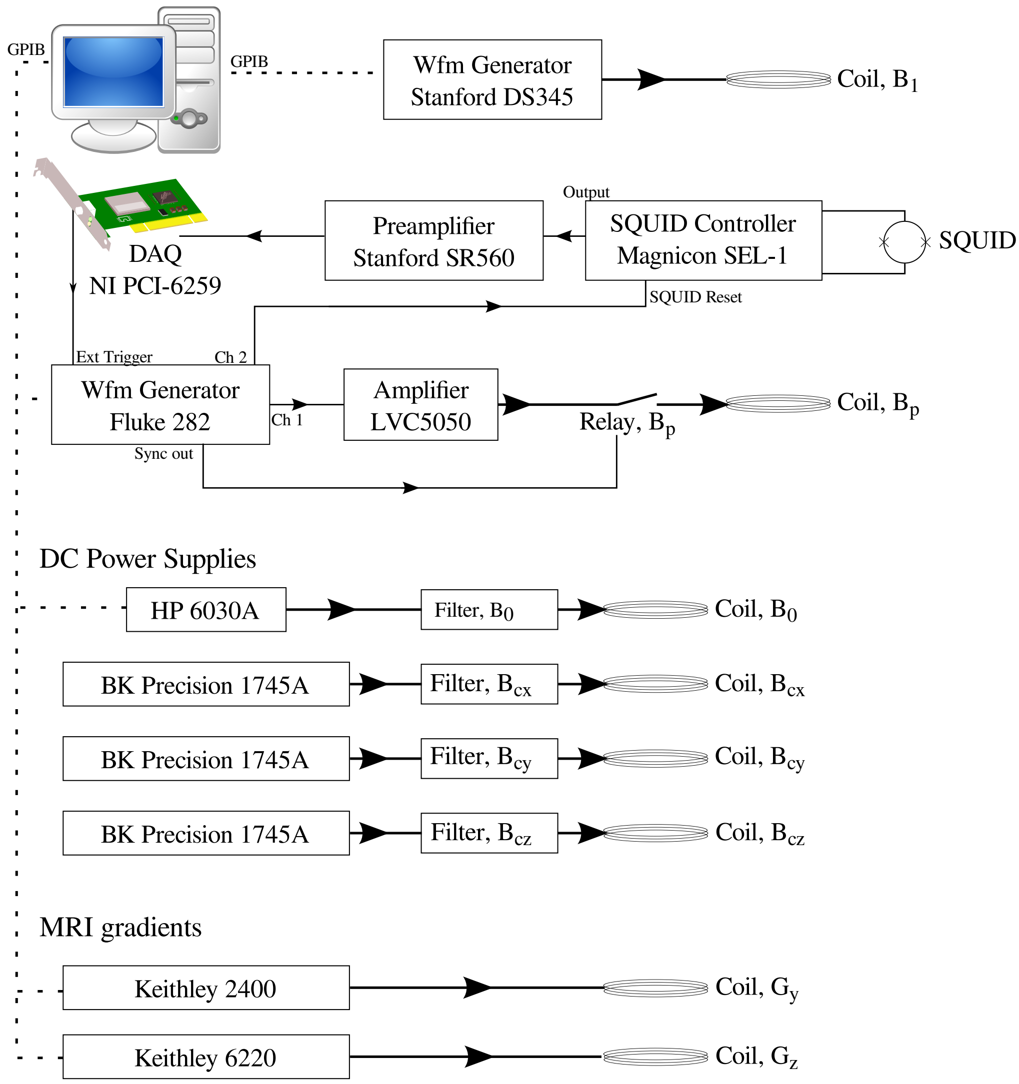

Figure 17: Schematic of the measurement setup for NMR and MRI experiments.

5.2 Results & Discussion

Our first discovery was that the $\mathbf{B_0}$ field needs to be kept constant, i.e. switching the $\mathbf{B_0}$ field as suggested by Zotev et al. is impractible for our setup. The inductance of the $\mathbf{B_0}$ coil is 105 mH, which makes the step response of an applied voltage slow, over 100 ms. When connecting the $\mathbf{B_0}$ coil to the LVC5050 amplifier instead, we were able to achieve a switch of the $\mathbf{B_0}$ field direction in about 40 ms, but then it induced a voltage in the cancellation coils via mutual induction, which caused a 100 ms oscillation in those coils instead. The output from the amplifier was also a bit too noisy for our experiments.

The switching of the $\mathbf{B_0}$ field also made the SQUID unstable, and we were unable to lock it after a few pulses.

5.2.1 Configuration 1: Excitation sequences

When using the Helmholtz prepolarization coil, the highest prepolarization field achievable without the SQUID unlocking was 0.5 mT. This did not yield any noticable peak in the FFT, which seems to indicate that the field is too low. If we correct the simulations made earlier to account for the small coil experiments in section 4.3.2, we would need a field of 2 mT in order to get a distinguishable signal.

One approach to counteract the SQUID sensitivity may be to add an extra field cancellation loop that can be placed near the SQUID, like the one used in the solenoid coil. However, this cancellation loop might also affect the magnetic field in the sample, since they are both placed very close to the SQUID.

One other explanation to our weak signal may be that the excitation coil is too small, giving an inhomogenous field over the sample volume. This can possibly be resolved by simply using the Helmholtz prepolarization coil for both prepolarization and excitation, with an electronic circuit to switch between modes.

5.2.2 Configuration 2: Non-adiabatic turn-off of prepolarization pulse with unshielded SQUID

When using the solenoid prepolarization coil we were able to place a large water sample, held in a latex rubber container, inside the coil. When we added a cancellation loop to compensate for field inhomogenieties through the SQUID, we were able to prepolarize the sample reliably with a 9 mT field. We were also able to turn off the field in 150 μs, which satisfies the condition for non-adiabatic turnoff, $t < \frac{1}{f}$ [22], as described in section 2.6.

We produced a plausible NMR peak at 48 and 50 μT measurement field, which corresponds to Larmor frequencies at 2044 and 2146 Hz. Since the peaks were embedded into the noise, we decided that more experiments

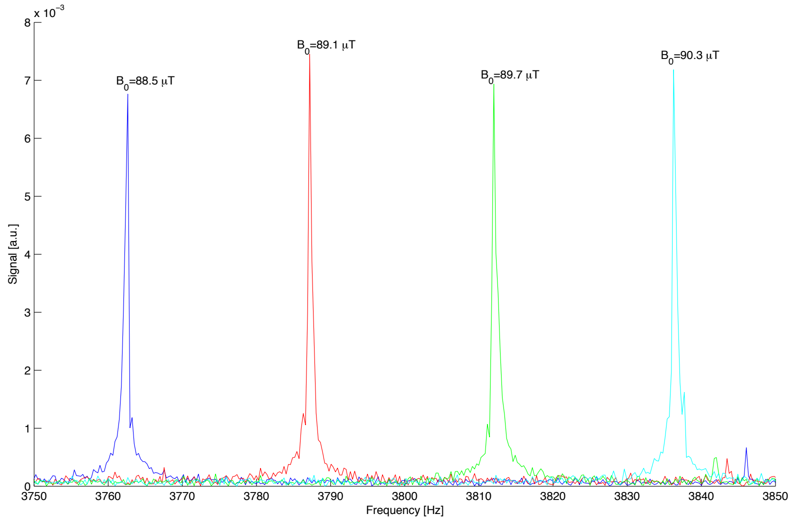

Figure 18: The single-shot NMR peaks for 4 different currents in the measurement coil, when using the shielded SQUID coupled to a copper transformer. Prepolarization of 18 mT, 12 ml of tap water, SNR=60.

would be needed to verify these results, so we instead tried using a copper flux transformer.

5.2.3 Configuration 3: NMR Results with copper transformer

The use of a copper pickup-coil made the difference for our measurements. We were able to prepolarize the sample in 18 mT field without needing any kind of careful alignment. Figure 18 shows the resonant peaks for a 12 ml water sample, taken at four slightly different strengths of the measurement field. The signal-to-noise ratio is 60 for a single shot.

The plot in figure 19 shows the dependence of the Larmor frequency on the current through the B_0-coil. We can see a clear linear relation between them. The fitted line is described by $f_L = 42.576 \times 118.58 \times I - 13$ Hz, where I is the current through the coil. Since the relation between current and field is linear, this means that the relation between the field and Larmor frequency also is linear, as expected. The offset of 13 Hz can be caused by an offset of 2mA in the current through the coil, which is at the limit of the accuracy of the power supply.

5.2.4 Simultaneous fluxgate measurements

From our investigations of the magnetic fluctuations we know that the magnetic field fluctuates in the order of 200 nT. We soon discovered that this

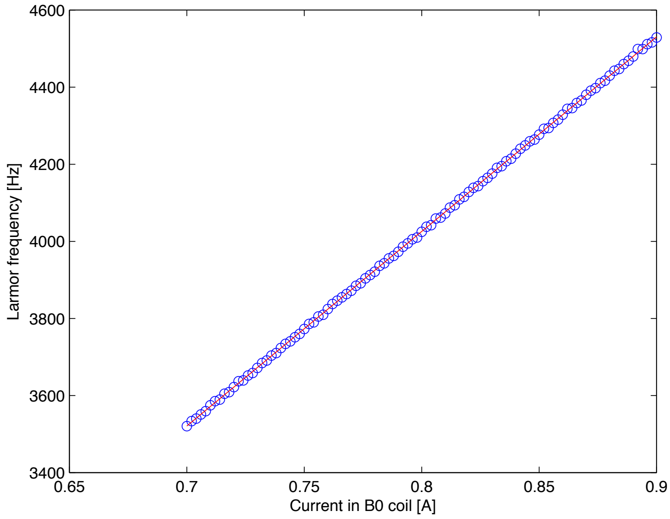

Figure 19: The frequency of the NMR peak compared to current in the B_0-coil. We see a clear linear response. 10 ml sample, Prepolarization field of 15 mT.

translated into a movement in the resonant peak of up to 10 Hz between measurements. This means that averaging is not as efficient, since the peak is smeared over a range of frequencies, resulting in a broader final peak.

By simultaneously using a fluxgate magnetometer to measure the variations of the magnetic field, and shifting the individual spectra accordingly, we were able to decrease the linewidth of the NMR peak from 4.5 Hz to 0.9 Hz. The peak movement between different measurements is shown in figure 20, whereas figure 21 shows a comparison between normal averaging and averaging with this peak alignment.

For more advanced pulsing sequences, and 3D imaging we will need the magnetic field to be stable, so in the long run we will need active compensation for the fluctuations, but in the meantime this kind of alignment seems to be helping a lot.

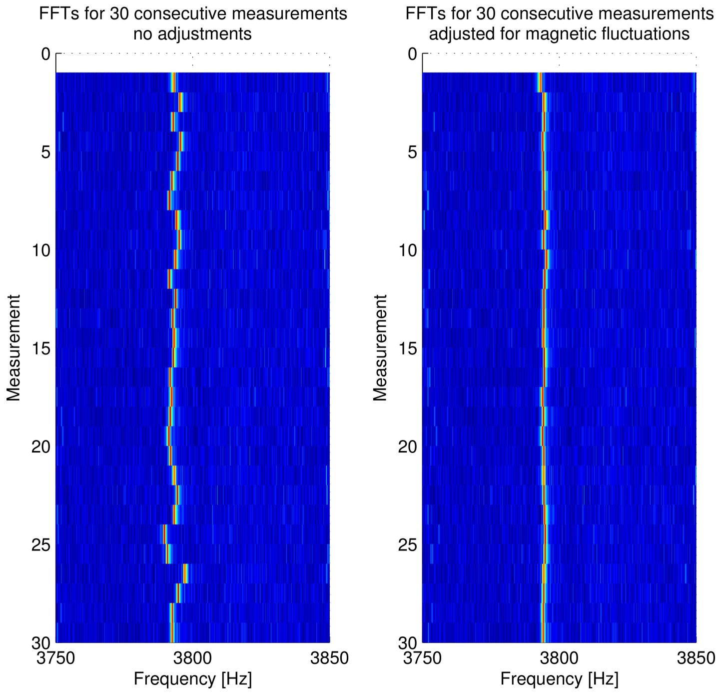

Figure 20: A view of the position of the resonant peak for each individual measurement before and after compensation for the magnetic fluctuations. Total time for all 30 measurements is 300 s.

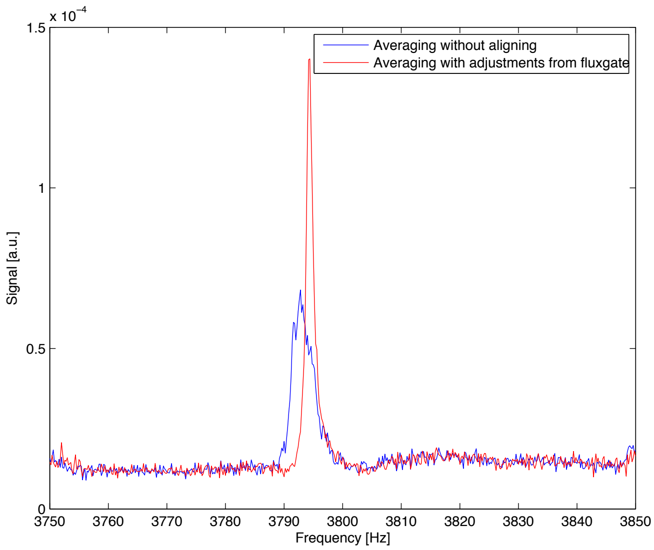

Figure 21: Comparison of the average resonant peak for a 10 ml sample with and without compensation for the magnetic fluctuations.

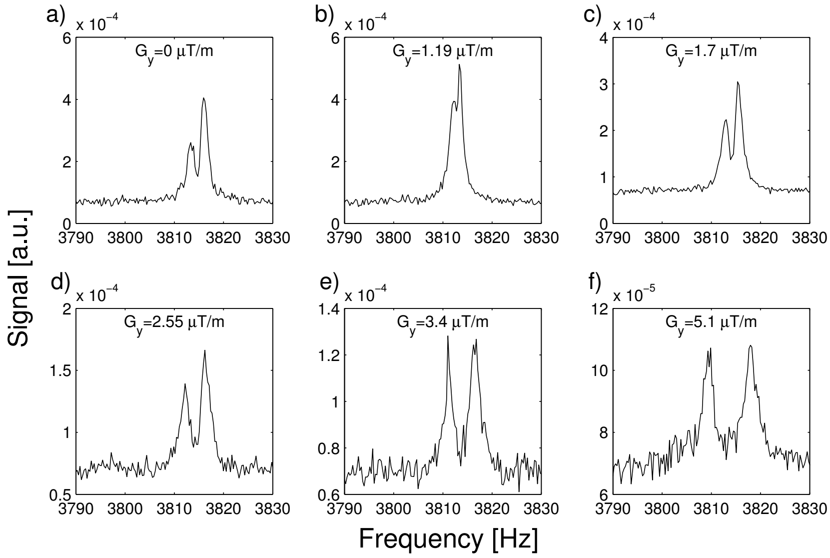

Figure 22: NMR signal of a sample consisting of two 3 ml water samples placed 4 cm apart with varying strength of the applied gradient field. We see that the peaks first combine, and then move further apart when increasing the gradient field. This implies that there is a residual gradient field in the system.

5.2.5 1D imaging with copper transformer

We placed two water samples (3 ml each) at a separation of 4 cm inside the pickup coil. We then applied a gradient field in the $\hat{\mathbf{y}}$-direction and studied the resonant spectrum at different gradient strengths. Figure 22 shows the results, where we see that we first have two peaks when not applying any gradient. When increasing the gradient, we first see the peaks moving together, and then separate at higher gradient fields. This suggests that there already is a gradient present in the system, which is probably caused by one of the earth cancellation coils. There has not been time to investigate this matter further, but as a temporary fix we moved the small coil setup (gradient coils, prepolarization coil and copper pickup-coil) 8 cm in the $\hat{\mathbf{y}}$-direction which caused the external gradient to disappear.

5.2.6 2D imaging with copper transformer

We have made a few attempts to use our system for imaging water phantoms in two dimensions. To decrease the complexity of the experimental setup, We used the backprojection method described in section 2.7. We placed a 7.5 cm long cylinder (2 cm in diameter) in the middle of the measurement system. To get as high signal strength as possible We placed the cylinder vertically (in the $\hat{\mathbf{x}}$-direction), and applied gradients in the $\hat{\mathbf{y}}$- and $\hat{\mathbf{z}}$-direction. Each point in the 2D image then represents a column of water in reality, which means that we image a cross-section of the cylinder. By performing measurements with the 1D gradient, We deduced that the highest gradient field strength possible in order to get a reasonable SNR for this setup was $|G| = |G_y\hat{\mathbf{y}} + G_z\hat{\mathbf{z}}|$=10 μT/m. We used a prepolarization field strength of B_p=19 mT and made 24 projections at 15° increments. Each projection contained the average spectrum from 25 measurements.

We also tried two other shapes of the cross-section in order to verify the results. Figure 23 displays the cross-section of the water phantoms and the resulting images.

In the top image we see that the sensitivity of the pickup coil is not uniform and the signal is a bit lower in the middle of the cylinder. This seems reasonable, since simulations show that field lines from a magnetic dipole near the center close inside the cylinder, so we get a lower net flux compared to a dipole near the edge of the cylinder. We can also use these results as a sensitivity profile for the coil, and use it to correct the other images, but so far this has not made any significant difference.

When looking at the other two shapes, we see that the imaging capabilities of the system so far is quite rudimentary, and should mostly be seen as a proof-of-principle. The edges are blurred, which is caused by several contributing factors. As discussed in section 2.7, the back-projection method introduces blurring in itself, but the main part is most probably caused by the magnetic fluctuations. Even with the fluxgate compensation, the error in the resonant frequencies is within 1 Hz. The width of the sample in the image is roughly 20 Hz, and each pixel is 0.4 Hz so the resulting image is smeared by a few pixels in each direction. This makes me estimate the resolution of the system to 2x2 mm, which corresponds to a voxel volume of 0.3 cm^3. A quick calculation from the NMR measurements, where 12 ml water gave us an SNR=60, would mean that the smallest detectable volume in a single shot is 0.2 cm^3, so the resolution seems reasonable. On the other hand, averaging the signal from several measurements has less of an impact than expected, which is probably caused by the magnetic fluctuations.

Another cause of the errors is that the water cylinder is quite large compared to the gradient coils. This means that the inhomogeniety of the gradient field in the vertical direction also can give rise to an error of the signal. This basically means that we get a slightly distorted image from each cross-section of the cylinder, resulting in a blurred total composition.

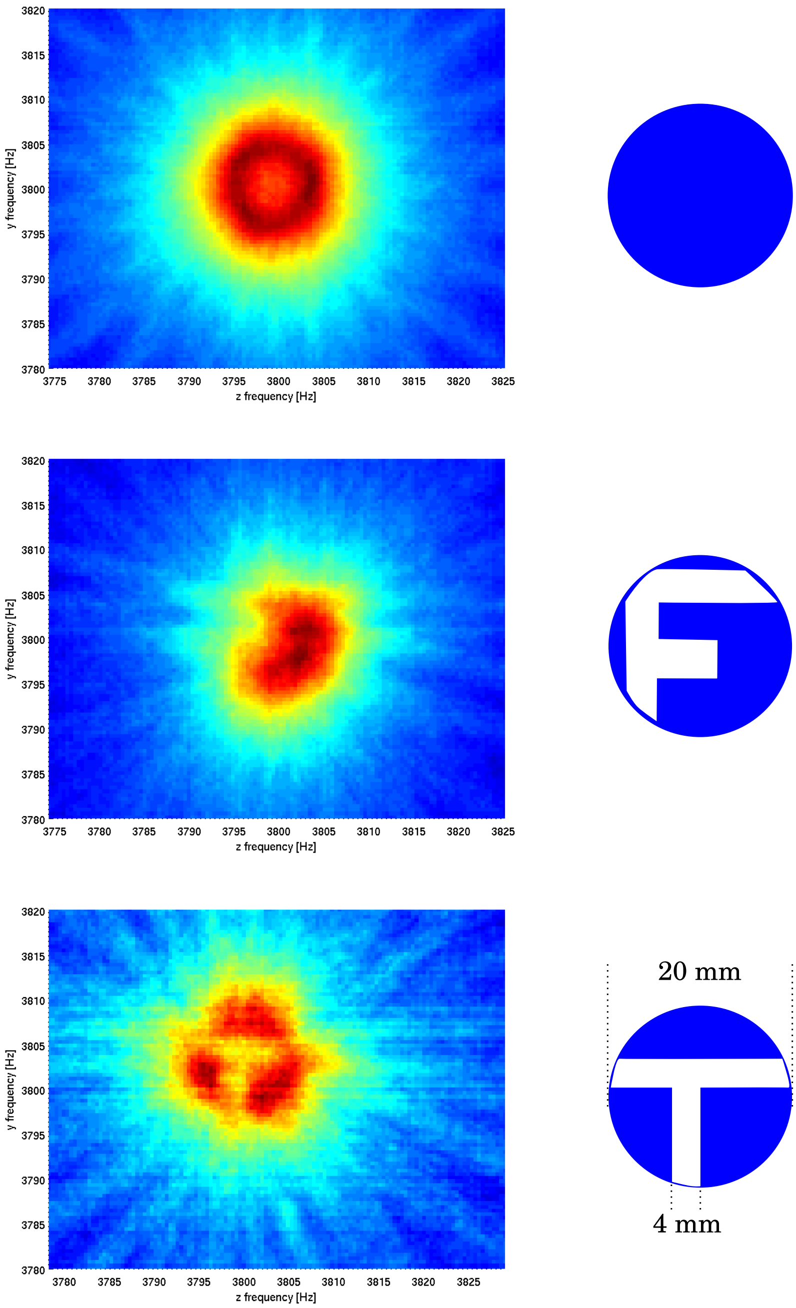

Figure 23: The images describe the imaged signal compared to the shape of the water phantom. The top images show our reference cylinder of water. The middle images show a phantom shaped like an F, and the bottom images show a phantom shaped like a T. Note that the position of the T-symbol in the MR image is slightly off-center, which is caused by the fluctuations of the magnetic field for the first measurement.

6 Conclusions

The imaging capabilities of our system have been demonstrated on three different water phantoms and the smallest detectable volume has been determined to be 0.3 cm^3. An NMR spectrum for a water sample at several different measurement fields has been recorded with the help of a resonant copper flux transformer, and the frequency of the resonant peak has been verified to coincide with the Larmor frequencies. The signal-to-noise ratio of a single shot of 12 ml water sample has been determined to be 60 and the linewidth (full width at half maximum) of the resonant peaks are 0.9 Hz.

Simulations for the signal strength in a high-T_c SQUID gradiometer have been performed, and show that we need a slightly higher prepolarization field in order to directly measure the NMR signal (without copper transformer).

There are several improvements that can be made in order to continue the work with NMR and MRI, which I will discuss further.

6.1 SQUID development

On the SQUID side, we first need to do a proper investigation of the SQUID gradiometer, where we need to find the cause of the sudden increase in sensitivity when increasing the field directed vertically into the SQUID plane. An investigation of the flux dam design might also need to be done, in order to establish that they work as intended.

We have seen that pulsing the magnetic field with unshielded SQUIDs leads to flux trapping in the film. The only way to rectify this problem is to heat up the SQUID above the transition temperature, and cool it down again. Another master thesis is focusing on achieving this quickly, in the order of milliseconds [25]. When finished, this work will need to be integrated into the MRI setup since some way of protecting the SQUID is needed for higher prepolarization fields.

In low-T_c SQUIDs the use of a superconducting flux transformer connected to a 2nd order axial gradiometer is possible. In the high-T_c field on the other hand, a lot of progress has yet to be made. Some promising work on a superconducting flux transformer has been made, but the inflexible nature of the YBCO material makes these efforts a lot more complicated than for its low-T_c counterpart.

6.2 Fluctuations of external magnetic field

At the moment we need to do measurements when they are most favorable, which means weeknights between 02:35 and 03:35. We have worked around this problem by simultaneously measuring the magnetic fluctuations and compensating for them when post-processing the signal, but since we still get a residual error this method does not seem to be a sustainable solution.

Active compensation on the earth cancellation coils can rectify this problem, but in order to get this working there are a lot of problems to be solved, such as how to shield it from the pulsing fields during the experiments.

6.3 Coil development

Since the amplifier used to drive the prepolarization coil has a quite noisy output, one approach to reducing noise levels might be using batteries as a power supply instead. Of course, this has the disadvantage of putting a time limit on each experiment.

Using the solenoid prepolarization coil works at the moment, but it is already heating the sample and higher field strength will be necessary to increase the signal. It is also far from ideal for imaging, since it needs to have a larger diameter in order to fit a more realistic phantom inside. Another possible improvement is using liquid nitrogen to lower the resistance of the coil, allowing for a larger prepolarization current.

If we want to continue our work on MRI with a copper flux transformer, there are also a lot of improvements to be made on the pickup coil. For example, the quality factor of the coil is very low, 5.5, which we should be able to improve with a different type of wire, and lower AC resistance. Enpuku et al. [32] have shown that by using Litz wire and cooling the coil with liquid nitrogen, they were able to construct a resonant coil with a quality factor of 135.

6.4 Gradient fields

First, we need to find the source of the stray gradient field in the $\hat{\mathbf{y}}$-direction. Larger gradient coils might also need to be constructed in order to improve uniformity of the applied gradient field. At the moment, no filters are used on the coils, which might introduce additional noise. Using batteries as a power supply for the gradient coils did not have any significant effect on the noise levels, but as sensitivity of the system improves in the future filters might be needed.

References

[1] J. Clarke, M. Hatridge, and M. Mößle, 'SQUID-Detected Magnetic Resonance Imaging in Microtesla Fields', *Annual Review of Biomedical Engineering*, vol. 9, August 2007, pp. 389-413

[2] H. C. Seton, D. M. Bussel, J. M. S. Hutchison, I. Nicholson and D. J. Lurie, 'DC SQUID based NMR detection from room temperature samples', *Phys. Med. Biol.*, vol. 37, 1992, pp. 2133–2138,

[3] H.C. Seton, J.M.S. Hutchison, D.M. Bussell, 'A 4.2 K receiver coil and SQUID amplifier used to improve the SNR of low-field magnetic resonance images of the human arm', *Meas. Sci. Technol.*, vol. 8, 1997, pp. 198-207

[4] R. McDermott,A. H. Trabesinger, M. Muck, E. Hahn, A. Pines and and J. Clarke, 'Liquid-State NMR and Scalar Couplings in Microtesla Magnetic Fields', *Science*, vol. 295, 2002, pp. 2247-2249

[5] J. Clarke, Interview with F. Pulizzi, 'SQUIDs for everything' *Nature Materials*, 10 , 2011, pp. 262–263

[6] M. Mößle, S. Han, W. Myers, S. Lee, N. Kelso, M. Hatridge, A. Pines, J. Clarke, 'SQUID-detected microtesla MRI in the presence of metal', *Journal of Magnetic Resonance*, vol. 179, Issue 1, March 2006, pp. 146-151

[7] V. S. Zotev, A. N Matlashov, P. L. Volegov, I. M. Savukov, M. A. Espy, J. C. Mosher, J. J. Gomez and R. H. Kraus Jr, 'Microtesla MRI of the human brain combined with MEG', *Journal of Magnetic Resonance*, 194, 2008, pp. 115–120

[8] Department of Homeland Security, *The Magnetic Vision Innovative Prototype (MagViz)*, Web. January 2011, URL: `http://www.dhs.gov/files/programs/gc_1265220854612.shtm`

[9] J. Garding, Elekta AB, Presentation at Imaging R & D in Western Sweden, Gothenburg, 30 Sep. 2010

[10] A. Abragam, *The principles of nuclear magnetism*, Oxford University Press,Oxford, 1961.

[11] Charles P. Slichter, *Principles of magnetic resonance*, Springer-Verlag,New York, 3rd edition, 1990

[12] Mark E. Haacke, Robert W. Brown, Michael R. Thompson, Ramesh, Venkatesan, Mark E. Haacke, Robert W. Brown, Michael R. Thompson, and Ramesh Venkatesan, *Magnetic Resonance Imaging: Physical Principles and Sequence Design*, Wiley-Liss, 1st edition, June 1999

[13] F. Bloch, 'Nuclear Induction', *Physical Review*, vol. 70, 1946, pp. 460–474

[14] E. Hahn, 'Spin Echoes', *Physical Review*, vol. 80, 1950, pp. 580–594

[15] B.F. Melton, V.L. Pollak, T.W. Mayes, and B.L. Willis, 'Condition for Sudden Passage in the Earth's-Field NMR Technique', *Journal of Magnetic Resonance*, Series A 117, 1995, pp. 164-170

[16] L. Q. Qiu, Y. Zhang , H.-J. Krause , S. Hartwig , M. Burghoff and L. Trahms 'Liquid state nuclear magnetic resonance at low fields using a nitrogen cooled SQUID', *Appl. Phys. Lett.*, vol. 90, 2007, pp. 182503,

[17] V. S. Zotev, A. N Matlashov, P. L. Volegov, A. V. Urbaitis, M. A. Espy and R. H. Kraus Jr, 'SQUID-based instrumentation for ultralow-field MRI', *Supercond. Sci. Technol.*, 20, 2007, S367-73

[18] R. McDermott,S. Lee, B. Haken, A. H. Trabesinger, A. Pines and J. Clarke, 'Microtesla MRI with a superconducting quantum interference device', *Proc. Natl. Acad. Sci.*, USA 101, 78577861, 2004

[19] Pascone, R.; Vullo, T.; Cahill, P.T.; and A. Tankhiwale, 'Theoretical And Experimental Analysis Of Magnetic Field Gradients For MRI' *Nuclear Science Symposium and Medical Imaging Conference*, Nov 1993, IEEE Conference Record, pp. 1349-1353

[20] R. C. Gonzalez and R. E. Woods, *Digital Image Processing*, Upper Saddle River, Pearson Prentice Hall, 2008

[21] J. R.Waldram, *Superconductivity of Metals and Cuprates*, Bristol, Institute of Physics Pub., 1996.

[22] W. Myers, D. Slichter, M. Hatridge, S. Busch, M. Mößle, R. McDermott, A. Trabesinger and J. Clarke, 'Calculated signal-to-noise ratio of MRI detected with SQUIDs and Faraday detectors in fields from 10 μT to 1.5 T', *Journal of Magnetic Resonance*, vol. 186, Issue 2, June 2007, pp. 182-192,

[23] D. Drung, 'High-Tc and Low-Tc Dc SQUID Electronics.', *Superconductor Science and Technology*, 16.12, 2003, pp. 1320-336

[24] R. H. Koch, W. Eidelloth, B. Oh, R. P. Robertazzi, S. A. Andrek, and W. J. Gallagher, 'Identifying the source of 1/f noise in SQUIDs made from high-temperature superconductors', *Appl. Phys. Lett.*, 60, 1992, 507

[25] H. A. Tash, *'Fast de-Trapping of Magnetic Flux From High Temperature Superconducting Devices'*, MS Thesis, Chalmers University of Technology, Gothenburg, 2011, Print

[26] M. Burghoff; S. Hartwig; W. Kilian; A. Vorwerk; L. Trahms; , 'SQUID Systems Adapted to Record Nuclear Magnetism in Low Magnetic Fields', *IEEE Transactions on Applied Superconductivity*, vol. 17, no.2, June 2007, pp. 846-849

[27] National Instruments Corporation, *NI 625X Specifications*, Web. June 2007, URL: `http://www.ni.com/pdf/manuals/371291h.pdf`

[28] E.R. Javor; T. Anderson, T, 'Design of a Helmholtz coil for low frequency magnetic field susceptibility testing', *Electromagnetic Compatibility, 1998. 1998 IEEE International Symposium on*, vol. 2, pp. 912-917, 24-28 Aug 1998

[29] S. Mak, 'Six ways to measure inductance', *Phys. Educ.*, vol. 37, 2002, pp. 439

[30] S. Liao, H. Yang, H. Horng, S. Yang, H. Chen, D. Hwan and L. Hwang 'Sensitive J-coupling spectroscopy using high-Tc superconducting quantum interference devices in magnetic fields as low as microteslas' *Supercond. Sci. Technol.*, vol. 22, 2009

[31] F. Öisjöen, *'High-T_c SQUIDs for biomedical applications: immunoassays, MEG, and ULF-MRI'*, Ph.D Thesis, Chalmers University of Technology, Gothenburg, 2011, Print

[32] K.Enpuku, S. Hirakawa, R. Momotomi, M. Matsuo, and T. Yoshida, 'Performance of HTS SQUID using resonant coupling of cooled Cu pickup coil' *Physica C: Superconductivity*, vol. 471, Issues 21-22, November 2011, pp. 1234-1237

Appendices

A Project description

Introduction

MRI

MRI has proven to be a useful tool in medicine for studying the soft tissue inside the body. It is based on the principle of Nuclear Magnetic Resonance (NMR), which says that the Larmor frequency of protons depends on the strength of the magnetic field. By creating a gradient magnetic field, each point in space yield a specific Larmor frequency, which can be used to create an image. The Faraday detectors used in a conventional MRI have a high sensitivity at high frequencies, which means that high magnetic fields are required ($\sim$2 T).

By using a SQUID (Superconducting Quantum Interference Device), we are able to detect small variations in the magnetic field at lower frequencies ($\sim$10 kHz), which in turn means that the required magnetic field can be much lower ($\sim$10 mT).

MEG

MEG (Magnetoencephalography) is a method of measuring brain activity. The current in active neurons give rise to a magnetic field, which can be registered with a SQUID. Since we are measuring the direct effect of brain activity this method is faster compared to functional MRI.

Purpose

By constructing an ulf-MRI system we will be able to combine MEG and MRI measurements in a single system. This means a possibility to map the brain activity directly on an image of the brain structure, which is not possible with conventional MEG. This thesis will mostly concentrate on the ulf-MRI part, since some progress already has been made on the MEG side.

By using high-Tc SQUIDs it will be sufficient to use liquid nitrogen cooling, which combined with the lower magnetic fields reduces the cost significantly compared to conventional systems. Since this also means thinner insulation for the SQUID, it will be closer to the head which possibly will make up for the decreased sensitivity of the high-Tc SQUID compared to its low-Tc competition.

Goal

The goals of the thesis are the following:

- Construct a proof-of-concept NMR system for studies of small samples.
- Evolve imaging capabilities in 1 dimension by adding a gradient coil to the system and develop data analysis methods for image reconstruction.

Further developments are possible if time allows:

- Combine MRI and MEG measurements in a single system, which includes construction of larger coils and cooling of coils.
- Add more gradient coils and pulse sequencing to achieve 3D imaging combined with MEG acquisition. This step is probably out of reach.

Method

The methods used will include but are not limited to:

- In-depth literature study of existing ulf-MRI systems.
- Design, building and testing electronic circuits for controlling the system.
- Setup of measurement rig, acquisition software and data analysis.
- Simulation of magnetic fields for design of coils.
- Some SQUID development might be needed in order to further increase sensitivity